

Morphology characterization and discrete element modeling of coral sand with intraparticle voids

Shuai Huang^a, Linchong Huang^{b,e}, Zhengshou Lai^{a,c,e,*}, Jidong Zhao^{c,d}

^a School of Intelligent Systems Engineering, Shenzhen campus of Sun Yat-sen University, Shenzhen 518107, China

^b School of Aeronautics and Astronautics Engineering, Shenzhen campus of Sun Yat-sen University, Shenzhen 518107, China

^c Department of Civil and Environmental Engineering, The Hong Kong University of Science and Technology, Hong Kong, China

^d HKUST Shenzhen-Hong Kong Collaborative Innovation Research Institute, Shenzhen 518045, China

^e School of Civil Engineering, Sun Yat-sen University, Zhuhai 519082, China

ARTICLE INFO

Keywords:

Coral sand
Intraparticle voids
Discrete element modeling
Signed distance field
Spherical harmonics
Level set

ABSTRACT

Coral sand is the main geomaterial on tropical reefs and its constituent particles are featured with complex shapes and abundant intraparticle voids. This work presents a discrete element method (DEM)-based numerical modeling of coral sand in consideration of both the irregular shape and intraparticle voids of particles. To develop the DEM model for coral sand, the acquisition and characterization of coral sand particles are first introduced. A signed distance field-based DEM applicable to arbitrarily irregular-shaped particles is then presented, in conjunction with two versatile particle models, namely spherical harmonics (SH) and level set (LS). To generate virtual coral sand particles that conform to target morphology characteristics, the combined random field and SH approach and the remedy to elongated particles are also presented. The developed DEM model is calibrated and validated against laboratory column collapse tests, where the agreements between numerical simulations and laboratory experiments demonstrate the good validity and accuracy of DEM model for coral sand. The performance of SH and LS particle models are also compared, providing a useful reference for the selection of appropriate particle models for coral sand in practice.

1. Introduction

Coral sand is a special type of geomaterial that is widely distributed on tropical islands and reefs (e.g., the South China Sea, the Persian Gulf, and the Red Sea) (Pac, 1978; Alba and Audibert, 1999). It is mainly formed by the metabolism product (e.g., calcium carbonate) and skeletons of corals after complex mechanical processes of ocean waves. Comparing with terrigenous quartz sand, the morphology of coral sand is featured with two characteristics, namely high complexity of shapes and full development of intraparticle voids (Wang et al., 2020a; Zhou et al., 2020a). Such characteristics substantially affect the mechanical and engineering properties of coral sand. For example, it has been shown that the shape irregularity of coral sand is the main cause of the particle obstruction mechanism, which results in shear dilation and increased shear strength under low loading conditions (Wang et al., 2019a). Under high loading conditions, coral sand exhibits a high susceptibility to breakage, where the intraparticle voids play an important role (Lv et al., 2021). Coral sand thus is of high compressibility, which has brought

extreme challenges in the design and construction of North Rankin A in the 1980s (King, 1980). With growing need of constructing infrastructures on tropical islands and reefs, both experimental (Lade et al., 2009; Wang et al., 2011; Salem et al., 2013; Shahnazari and Rezvani, 2013; Wang et al., 2017; Rui et al., 2020; Ma et al., 2022; Xiao et al., 2022) and numerical (Yu et al., 2020; Wu et al., 2021; Shi et al., 2021a; Hu et al., 2021; Lu et al., 2022; Xu et al., 2022; Qin et al., 2022) research efforts on coral sand have been on the rise recently. Developing a workflow for morphology characterization and the tool for numerical modeling of coral sand is essential to the fundamental understanding and application of coral sand in engineering.

To obtain the morphology of coral sand, a variety of imaging techniques are available, including photography (Wei et al., 2020; Wang et al., 2020b), scanning electron microscopy, stereophotography (Zheng and Hryciw, 2017), photogrammetry (Zhao et al., 2020), and X-ray computed tomography (CT) (Garboczi, 2011; Andò et al., 2013; Zhou et al., 2015). Among these techniques, the X-ray CT can directly obtain three-dimensional morphological information, including both particle

* Corresponding author at: School of Intelligent Systems Engineering, Shenzhen campus of Sun Yat-sen University, Shenzhen 518107, China.

E-mail address: laizhengsh@mail.sysu.edu.cn (Z. Lai).



Fig. 1. Photograph of two representative types, namely stick-like and lump-like, of coral sand particles.

apparent shapes and intraparticle voids and thus is gaining increasing popularity for morphology characterization of coral sand in recent years (Kong and Fonseca, 2018; Kong and Fonseca, 2019; Zhou et al., 2020b; Zhou et al., 2022). For example, based on X-ray CT, Zhou et al. (2020b), Zhou et al. (2022) presented a detailed quantitative study on the morphology and intraparticle pore structure and analyzed the crushing behavior of single coral sand particles; Kong and Fonseca (2019) investigated the evolution of the grain morphology and coordination number of bulk shelly carbonate sand under one-dimensional compression test. The successful application of X-ray CT to coral sand facilitates the developments of morphology-informed numerical models for coral sand. It is worth noting that, with raw images obtained from X-ray CT, image processing may be required to extract the information of interest (e.g., to identify and extract the data of individual particles). For coral sand particles with complex shapes and intraparticle voids, special image processing procedures, such as machine learning and level set enhanced particle reconstruction (Lai and Chen, 2019), can be adopted for improved performance.

From the continuum material perspective, existing studies on the modeling of coral sand include the finite element method (Yu et al., 2020; Qin et al., 2022) and finite difference method (Wu et al., 2021). For instance, Yu et al. (2020) studied the long-term settlement of an airport runway on a coral sand foundation using the finite element method with software ABAQUS. Qin et al. (2022) analyzed the effect of pile inclination on the lateral deformation behavior of pipe piles in coral sand using the random finite element method. Wu et al. (2021) studied the seismic response of soil-pile-superstructure in coral sand with the finite difference method. Coral sand is typically a discontinuous material, where the macroscopic behavior is governed by the movements and interactions of the constituent particles at the microscopic scale. Modeling coral sand with discontinuous methods from the microscopic scale is important to the investigation of micro-mechanisms of coral sand behavior and the derivation of mesoscale coral sand responses (e.g., the stress-strain constitutive relations) required for continuum modeling.

Currently, particle-wise numerical modeling of coral sand mainly includes discrete element method (DEM) and finite discrete element method (FDEM). DEM considers rigid particles and updates the motion of particles based on the Newton-Euler equation. When integrated with bonded particle model, DEM can be used to model particle breakage as well (Peng et al., 2018; Wang et al., 2019b; Kuang et al., 2021), whereas it is physically less accurate than FDEM. FDEM is a combination of finite element method (FEM) and DEM, where FEM is employed to model particle deformation as well as breakage, and DEM is utilized to approach the interactions between particles and fragments. For instance, using FDEM, Zhou et al. (2022) studied the breakage behavior

of single coral sand particles, where the intraparticle pore structure is substantially considered. Nonetheless, FDEM simulation is subject to extremely high computational expenses, making it unfeasible for modeling problems with many particles. In the cases of low loading conditions where coral sand particles exhibit little susceptibility to breakage, DEM becomes a preferred option. However, most existing DEM studies (Wang et al., 2019b; Kuang et al., 2021; Shi et al., 2021a; Xu et al., 2022) of coral sand used sphere or clump of spheres to model irregular-shaped coral sand particles, which is computationally expensive and poses some issues in contact behavior evaluation. Recent years have witnessed the developments of many advanced non-spherical particle models, such as level set (LS) (Kawamoto et al., 2016; Kawamoto et al., 2018) and spherical harmonics (SH) (Feng, 2021a; Capozza and Hanley, 2021; Wang et al., 2021a). In particular, LS employs a set of discrete signed distances to track the boundary between solid and void, making it capable to capture the intraparticle voids of a particle. Yet the performance of LS and SH particle models for DEM simulation of coral sand has not been well discussed in the literature.

Another aspect is that, coral sand particles could present with various shapes, while often only a limited number of particles could be scanned due to the high cost of X-ray CT. To create enough number of particles for numerical modeling, there needs to generate virtual particles that conform to the morphology characteristics of real coral sand samples. Researches on generating virtual particles for numerical modeling include (Mollon and Zhao, 2014; Zhou and Wang, 2017; Su and Yan, 2018; Wang et al., 2021b), where the approach of combined SH and random field (RF) theory has shown to be rather efficient and effective for such a task (Zhou and Wang, 2017). A notable limitation of the RF-SH approach is that it is only applicable to particles with a small elongation. When applied to notably elongated particles, SH would result in spurious defects such as tortuous surface near the particle equator and pole areas. In view of this aspect, this work will investigate the applicability of RF-SH approach to coral sand and develop the remedy for elongated particles. It should be also noted that recently there are attempts that utilize the machine learning tools to generate virtual particles. For example, Shi et al. (2021b) developed the deep neural network-based variational-autoencoder approach to randomly generate three-dimensional schistous sand particles. Particle information is encoded into a latent code that could be characterized by a multivariate distribution and a new particle could be generated by decoding a piece of randomly sampled latent code. The machine learning-based approach has the advantage that it is straightforward and directly applicable to any types of particles. A worthwhile noting limitation is that the present machine learning-based approach may require a great number of particle samples for training.

This work presents a DEM modeling of coral sand in consideration of both the irregular shape and intraparticle voids of particles. Specially, a unified signed distance field (SDF)-based DEM together with two versatile particle models, namely SH and LS, for coral sand will be introduced, and a RF-SH approach for generating virtual coral sand particles will be presented. The effects of intraparticle voids on the mechanical behavior of coral sand will be analyzed based on the SH and LS models. The rest of the paper is organized as follows. Section 2 describes the approach of acquisition and characterization of coral sand morphology. Section 3 introduces the formulation of SDF-based DEM, as well as the LS and SH particle models. Section 4 presents the RF-SH approach and the remedy for elongated particles. Section 5 reports the results of shape accuracy of SH and LS particle models, effectiveness of RF-SH approach, and DEM simulation of column collapse. Section 6 summarizes the concluding remarks.

2. Acquisition and characterization of coral sand morphology

2.1. X-ray CT and image processing

Coral sand could present various shapes, with two of the most

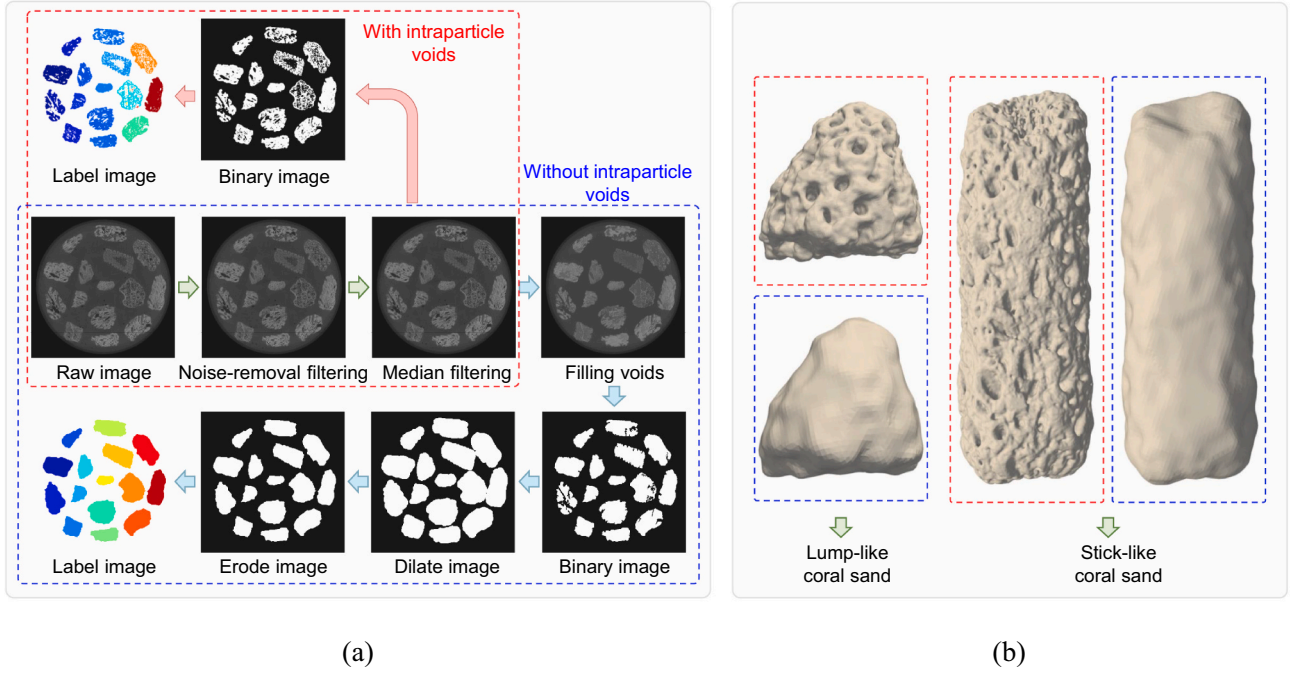


Fig. 2. Illustration of (a) the image processing procedure and (b) the final reconstructed particles represented by surface triangle mesh, for the cases with and without intraparticle voids.

representative ones being stick-like and lump-like, as shown Fig. 1. To obtain the morphology, a number of stick-like and lump-like coral sand particles are collected and filled in a cylindrical container prepared for X-ray CT scan. Specially, the particles are placed layer by layer with silicone gel being used to separate the particles, thus to avoid the challenge of image segmentation. The column of particles has a diameter and height of 50 mm, which yields 1250 stacks of raw CT images with a resolution of $40 \mu\text{m}$, i.e., $40 \mu\text{m}$ per voxel.

With the raw CT images, a series of image processing steps are performed to reconstruct the apparent shapes and intraparticle voids of particles. Fig. 2 illustrates the procedures of image processing and particle reconstruction. Specially, two schemes are considered with one including the particle intraparticle voids (marked with red in Fig. 2) and the other not (marked with blue). The former scheme retains the original microscopic pore structure of particles, whereas the latter one focuses on the overall profile of particles and could be favored by DEM simulations for the sake of computational efficiency. In this work, both the DEM simulations of coral sand particles with and without intraparticle voids will be conducted, and the effects of intraparticle voids on the mechanical behavior of coral sand will be analyzed. For both schemes, the raw images are first processed with a noise-removal filter followed by a median filter to enhance the image quality. Then, for the scheme with intraparticle voids, the images are binarized into solid and void phases, based on which a label filter is used to identify the owned voxels of each particle. It is noted that a two-dimensional slice image of coral sand is used to illustrate the labeling procedure in Fig. 2, whereas the labeling is performed on three-dimensional image data in implementation. A particle would contain several separated parts in a two-dimensional slice due to the abundance of intraparticle voids, whereas these separated parts are connected with each other and form a whole particle in the three-dimensions. Finally, the triangle surface mesh of each particle is constructed via the marching cube algorithm. For the scheme without intraparticle voids, additional dilation and erosion steps are performed to remove the voids inside particles. It is worth noting that the traditional filling-holes filter cannot achieve such a task due to the large size and abundance of voids. After filling intraparticle voids, particle surface is reconstructed using the marching cube algorithm. The image

processing schemes are implemented in MATLAB with recourse to build-in functions, including `wiener2`, `medfilt2`, `imfill`, `imdilate`, `imerode`, `bwlabeln`, and `isosurface`. Two examples of lump-like and stick-like particles with and without intraparticle voids are shown in Fig. 2b.

2.2. Characterization of particle morphology

With particle shapes reconstructed from CT images, various descriptors can be calculated to quantify the morphology of particles. In this work, the three commonly used particle morphology descriptors, namely aspect ratio (a_{yx} , a_{zx}), sphericity (S) and roundness (R), are adopted. Aspect ratio describes the form (e.g., flatness and elongation) of particles. To calculate the aspect ratio, a particle is first rotated to a standardized configuration, such that its principal axes, respectively, align with the x , y and z axes of the global coordinate system. Then, the axis-aligned bounding box of the particle is computed with the dimensions in each axis denoted as long length (L_x), intermediate length (L_y) and short length (L_z), respectively. Thereby, the aspect ratios are calculated as the ratio of short and intermediate lengths to long length, such that

$$a_{yx} = \frac{L_y}{L_x} \quad (1)$$

$$a_{zx} = \frac{L_z}{L_x} \quad (2)$$

The sphericity describes the degree to which a particle shape resembles a mathematically perfect sphere, and is calculated as the ratio of the surface area of an equal-volume sphere to the surface area of the particle, such that

$$S = \frac{(36\pi V_p^2)^{1/3}}{A_p} \quad (3)$$

where V_p and A_p are the volume and surface area of the given particle, respectively. Roundness generally refers to the relative sharpness of corners of particles, and is calculated as the average ratio of the curvature radius of all corners to the radius of the largest inscribed sphere of a

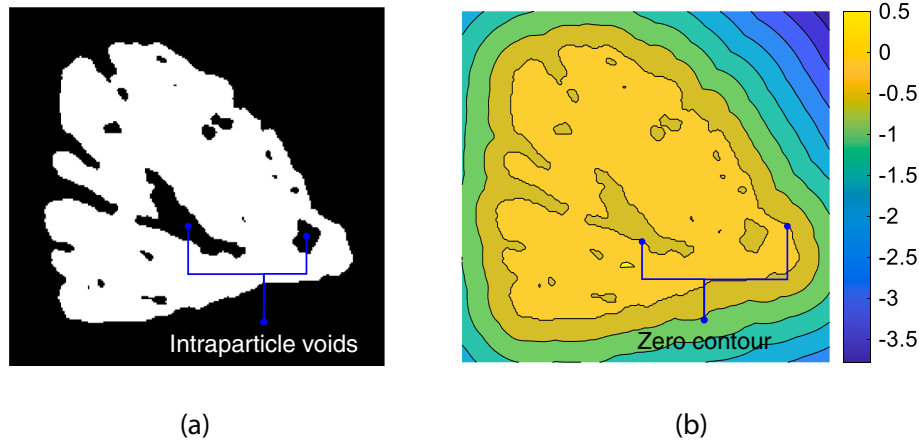


Fig. 3. Illustration of (a) the shape and intraparticle voids of a particle and (b) its representation by SDF.

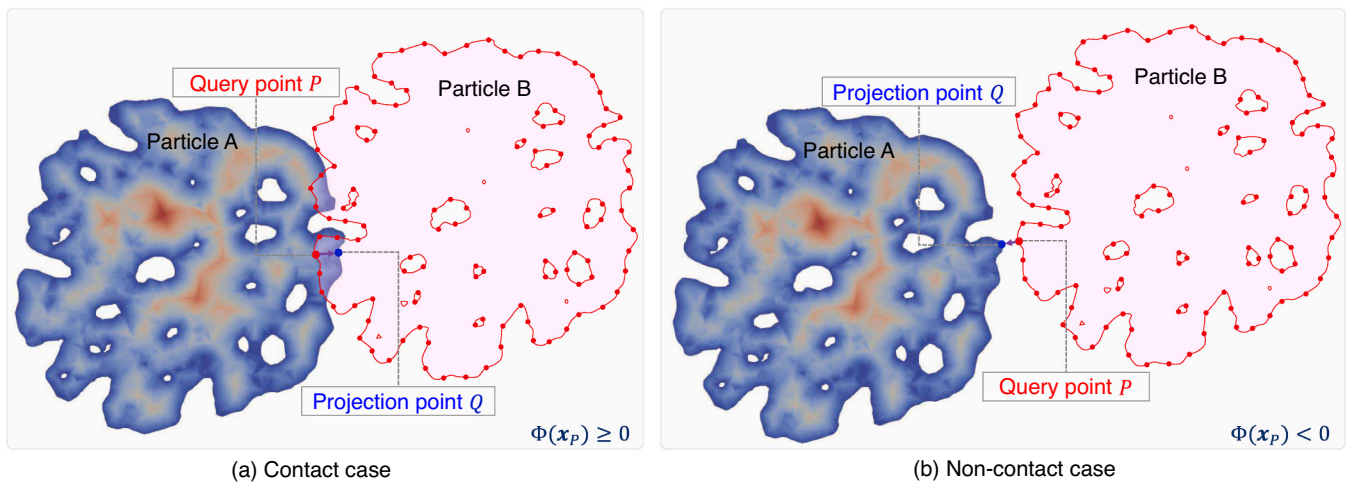


Fig. 4. Illustration of the node-to-surface algorithm for contact detection: (a) contact case and (b) non-contact case.

particle (Wadell, 1933; Zhou et al., 2018a)

$$R = \frac{\sum g(k) |k_{\max}|^{-1}}{NR_{\text{ins}}} \quad (4)$$

where R denotes the roundness; N is the total number of acceptable corners; R_{ins} is the radius of the maximum inscribed sphere of the particle; k_{\max} is the maximum curvature at a corner; and $g(k)$ is a function indicates whether a corner is acceptable or not, defined as

$$g(k) = \begin{cases} 1 & \text{if } |k_{\max}|^{-1} < R_{\text{ins}} \\ 0 & \text{if } |k_{\max}|^{-1} \geq R_{\text{ins}} \end{cases} \quad (5)$$

It should be pointed out that the sphericity and roundness are computed based on and thus characterize the morphology of the apparent shapes (i.e., shapes without intraparticle voids) of coral sand particles.

3. SDF-based DEM model for coral sand

3.1. SDF-based DEM

In the SDF-based DEM, particles are described by SDF, which is a continuous function $d = \Phi(x) : \mathcal{R}^3 \rightarrow \mathcal{R}$ that maps a spatial point x to a signed value d (Lai et al., 2022). In particular, different from the conventional definition of SDF (i.e., signed value d) which is the shortest distance from the query point to particle surface, the SDF-DEM adopts a broad-sense definition of SDF which can be either the shortest distance

from the query point to the particle surface, the radial distance from the query point to the particle surface, or any other distance that satisfy the condition that the SDF isosurfaces are non-self-intersection. An example of the SDF-based representation of particle is shown in Fig. 3. Without loss of generality, SDF is assumed to be positive for locations inside a particle and negative outside. The zeroth isosurface of SDF thus represents the particle surface. In addition to SDF function, the SDF-based particle model is furnished with a so-called surface projection function, which projects a point inside a particle onto the surface of the particle (see Fig. 4). The surface projection function will be used to determine contact points, which are required by contact models to evaluate contact forces and moments. Exact formulations of SDF will be presented in the subsequent section.

With particles described by SDF, node-to-surface contact algorithm is adopted to detect contacts and resolve contact geometric features. As illustrated in Fig. 4 for two particles (e.g., Particle A and B) being considered, the surface of Particle B needs first to be discretized into a set of surface nodes. Contact detection becomes to testing if any surface node on Particle B intrudes into Particle A. For contact resolution, the energy-conserving contact theory originally proposed by Feng (2021b) is adopted for evaluating the normal contact force, whereas the classical linear spring contact model with Coulomb friction law is adopted for the tangential frictional contact force. More specifically, the normal contact force is computed from the derivatives of a contact potential function with respect to particles' relative translation and rotation, as

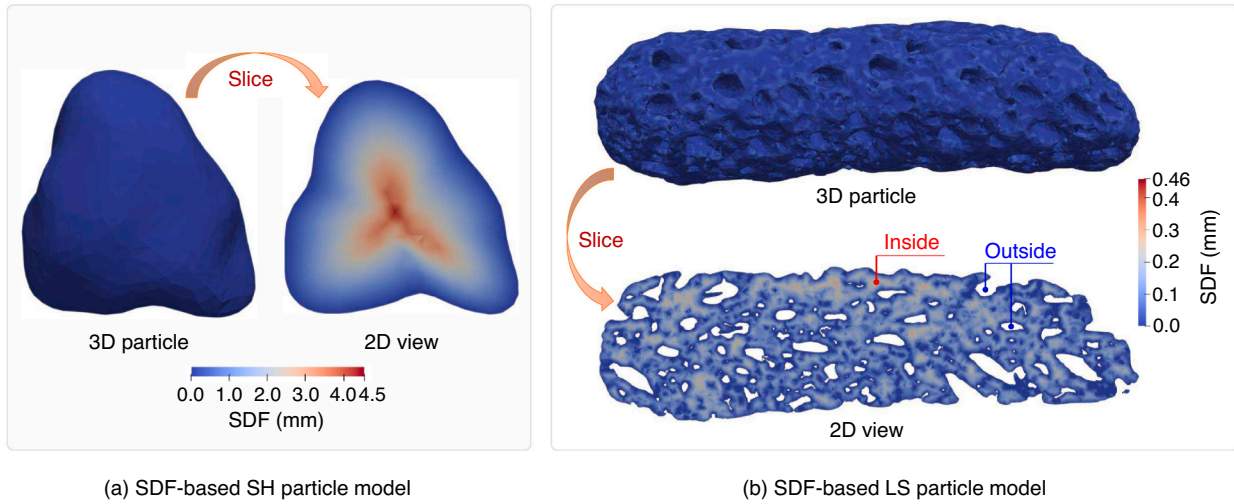


Fig. 5. Illustration of the two types of SDF-based particle model, namely SH particle model and LS particle model.

$$F_n = -\frac{\partial w(\mathbf{x}, \boldsymbol{\theta})}{\partial x} \quad (6)$$

$$M_n = -\frac{\partial w(\mathbf{x}, \boldsymbol{\theta})}{\partial \boldsymbol{\theta}} \quad (7)$$

where F_n and M_n are the normal contact force and moment, respectively, $w(\mathbf{x}, \boldsymbol{\theta})$ denotes the contact potential, and \mathbf{x} and $\boldsymbol{\theta}$ represents the relative position and rotation of Particle B with respect to Particle A. In this work, the contact potential is taken as

$$w(\mathbf{x}, \boldsymbol{\theta}) = \sum_{P_i \in B \rightarrow A} \frac{2k_n \mathcal{S}(d_i) S_B d_i}{\pi N_B d_B} \quad (8)$$

where k_n is the equivalent normal stiffness, d_i is the signed distance of intruding node i , S_B , N_B and d_B are the surface area, number of surface nodes and equivalent size of particle B, respectively, and $P_i \in B \rightarrow A$ represents the surface nodes of Particle B that intrude into Particle A. $\mathcal{S}(d_i)$ is a sigmoid function that satisfies $\mathcal{S}(0) = 0$ and $\mathcal{S}(d_{i,\max}) = 1$, and $d_{i,\max}$ represents the maximum permissible intrusion depth during a collision event. For the small contact theory in DEM, $d_{i,\max}$ is usually less than 5% of particle size. The sigmoid function implies that the contact volume associated with intruding node N_i is counted as zero when this node just starts to intrude into Particle A (i.e., $d_i = 0$), and is totally counted if the intruding depth become significant (i.e., $d_i = d_{i,\max}$). In this work, the following algebraic formulation of sigmoid function is adopted due to its computational efficiency

$$\mathcal{S}(d_i) = \frac{c_s d_i / d_B}{\sqrt{1 + (c_s d_i / d_B)^2}} \quad (9)$$

where c_s is a constant parameter that controls the shape of function, which is estimated as $c_s = 100$.

The tangential contact force is updated in an incremental manner, as

$$F_s = F_s^0 - k_t \delta_s \quad (10)$$

$$F_t = F_t^0 - k_t \delta_t \quad (11)$$

where F_s and F_t are the tangential contact forces in the tangential directions sand t , respectively; the superscript 0 indicates the tangential forces at the previous timestep; k_t is the contact tangential stiffness; and δ_s and δ_t , respectively, are the relative displacements in the contact tangential directions. The tangential contact force is tracked in two tangential directions to facilitate the transformation of contact frictional

force due to contact plane rotation (PFC documentation, 2021). To further incorporate the Coulomb's law of friction (Johnson, 1987; Balevičius and Mróz, 2013), the tangential contact forces are constrained as

$$F'_{st} = \min\left(\sqrt{F_s^2 + F_t^2}, \mu F_n\right) \quad (12)$$

$$F'_s = F'_{st} \frac{F_s}{\sqrt{F_s^2 + F_t^2}} \quad (13)$$

$$F'_t = F'_{st} \frac{F_t}{\sqrt{F_s^2 + F_t^2}} \quad (14)$$

where the symbol prime ' is used to indicate the updated tangential contact force based on the Coulomb's law of friction, F'_{st} is the total tangential contact force, and μ is the friction coefficient. It is worth noting that each intruding node will carry a contact force, and thus the total contact force needs to be added up from all the intruding nodes of two colliding particles. In this work, the SDF-DEM is implemented in our in-house DEM code and interested readers are referred to Lai et al. (2022) for more details.

3.2. Two types of particle models

Two formulations of SDF will be considered in this work, namely SH and LS. SH has been widely adopted by the geotechnical community for describing generally irregular-shaped particles due to its high accuracy and efficiency, whereas LS is superior in capturing the intraparticle voids of a particle, with the accuracy and efficiency highly dependent on the resolution of the level set grid though. Examples of SH particle model and LS particle model are shown in Fig. 5. The SDF function and surface project function for SH and LS are described as following.

3.2.1. Spherical harmonics (SH)

SH has been widely applied to model irregular star-shaped particles in three-dimensions (Mollon and Zhao, 2014; Zhou et al., 2015; Zhou and Wang, 2017; Zhou et al., 2018b). In SH, points on particle surface are described in spherical coordinates (r, θ, φ) , where r is the radial distance, and $\theta \in [0, \pi]$ and $\varphi \in [0, 2\pi]$ are the polar and azimuth angles, respectively. Mathematically, the radial distance r can be expressed as a SH expansion of $r(\theta, \varphi)$, that

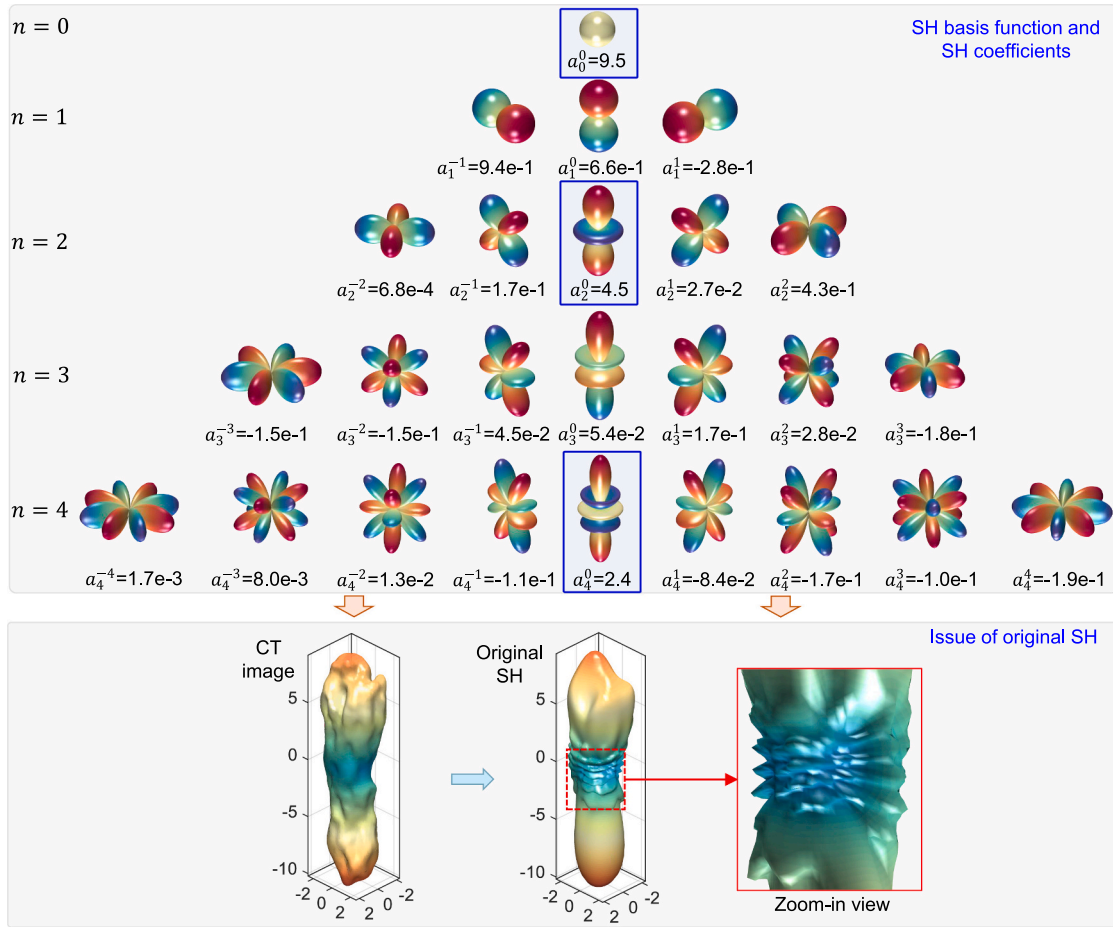


Fig. 6. Illustration of the issue of SH for modeling elongated particles. The top sub-figure shows the profile of SH basis functions and SH coefficients for fitting an elongated particle, and the bottom sub-figure shows the particle shapes reconstructed from CT and SH fitting, respectively.

$$r(\theta, \varphi) = \sum_{n=0}^N \sum_{m=-n}^n a_n^m Y_n^m(\theta, \varphi) \quad (15)$$

$$\Phi(x_p) = r(\theta_p, \phi_p) - \|x_p\| \quad (20)$$

3.2.2. Level set (LS)

LS relies on a grid of cells to calculate the SDF at every location. For a query point that resides in a certain cell, its SDF can be computed as the linear interpolation of the SDF at the cell nodes, such that

$$Y_n^m(\theta, \varphi) = \begin{cases} \sqrt{\frac{(2n+1)(n-|m|)!}{4\pi(n+|m|)!}} P_n^{|m|}(\cos\theta) \sin(|m|\varphi) & m < 0 \\ \sqrt{\frac{2n+1}{4\pi}} P_n^m(\cos\theta) & m = 0 \\ \sqrt{\frac{(2n+1)(n-m)!}{4\pi(n+m)!}} P_n^m(\cos\theta) \cos(m\varphi) & m > 0 \end{cases} \quad (16)$$

$$\Phi(x_p) = \sum_{a=0}^1 \sum_{b=0}^1 \sum_{c=0}^1 \Phi_{abc} [(1-a)(1-x) + ax][(1-b)(1-y) + by] [(1-c)(1-z) + cz] \quad (21)$$

$$P_n^m(x) = \frac{(-1)^m}{2^n n!} (1-x^2)^{m/2} \frac{d^{n+m}}{dx^{n+m}} (x^2-1)^n \quad (17)$$

where Φ_{abc} represents the SDF of the cell nodes with subscripts a, b and c indicating the node indexes; x, y and z are the local coordinates of point P and are calculated as

where N is the SH degree, n and m are the SH basis indexes, a_n^m is the SH coefficient, and $P_n^m(x)$ is the associated Legendre function.

$$x = (x_p - x_0)/l_x \quad (22)$$

To be integrated into SDF-DEM, the surface project function for SH is formulated as

$$y = (y_p - y_0)/l_y \quad (23)$$

$$\mathbf{x}_Q = (x_Q, y_Q, z_Q) = (cx_P, cy_P, cz_P) \quad (18)$$

$$z = (z_p - z_0)/l_z \quad (24)$$

with

where x_0, y_0 and z_0 are the coordinates of the lowest corner of the grid cell, and l_x, l_y and l_z are sizes of the grid cell in each dimension. The surface project function is given as

$$c = r(\theta_p, \phi_p) / \|x_p\| \quad (19)$$

where subscripts P and Q indicate the query point P and projection point Q , respectively; c is a scaling coefficient; and $\|x_p\|$ represents the Euclidean norm length of x_p . Then, the SDF function $\Phi(x_p)$ is defined as the distance between points P and Q that

$$\mathbf{x}_Q = (x_Q, y_Q, z_Q) = (x_p, y_p, z_p) - \Phi(x_p) \frac{\nabla\Phi(x_p)}{\|\nabla\Phi(x_p)\|} \quad (25)$$

where $\nabla\Phi(x_p) = (\nabla_x\Phi, \nabla_y\Phi, \nabla_z\Phi)$ represents the spatial gradient of

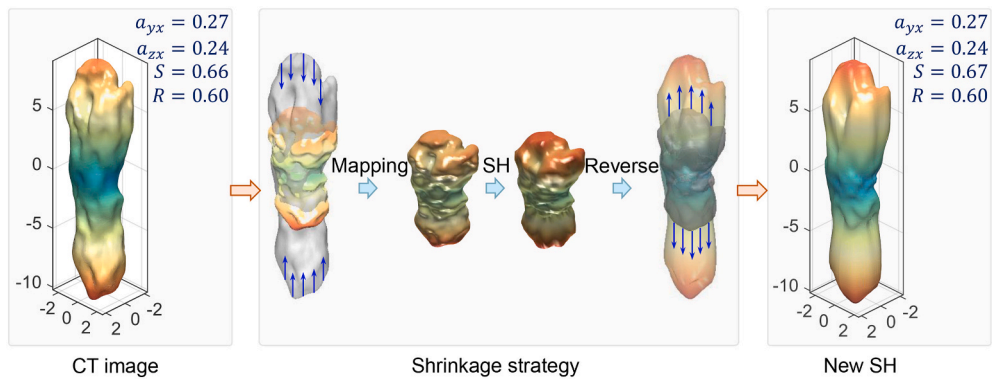


Fig. 7. Illustration of the shrinkage strategy to SH for modeling elongated particles.

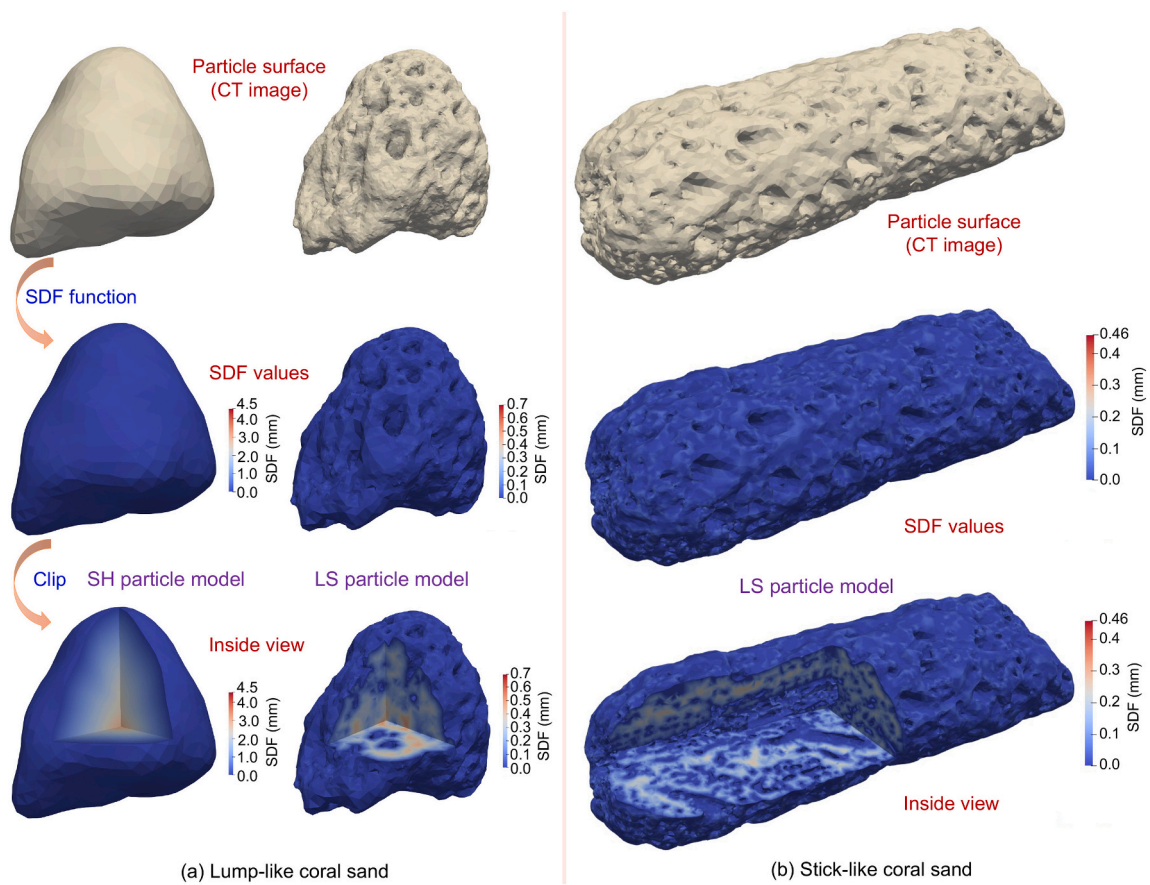


Fig. 8. Visualization of the SDF of (a) a lump-like coral sand particle and (b) a stick-like coral sand particle.

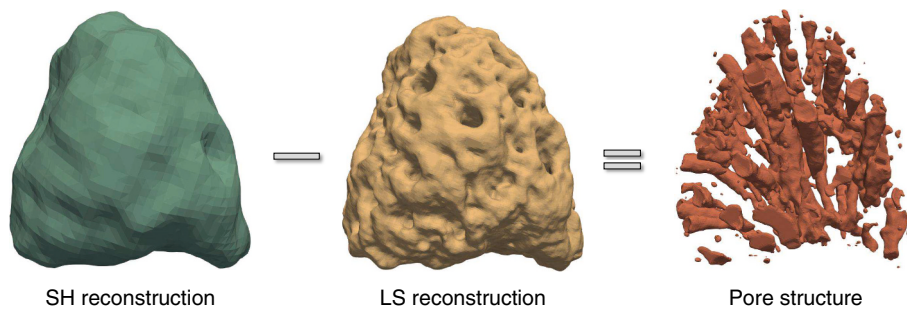


Fig. 9. Illustration of the difference between the SH particle and LS particle, and the micro-structure of internal voids.

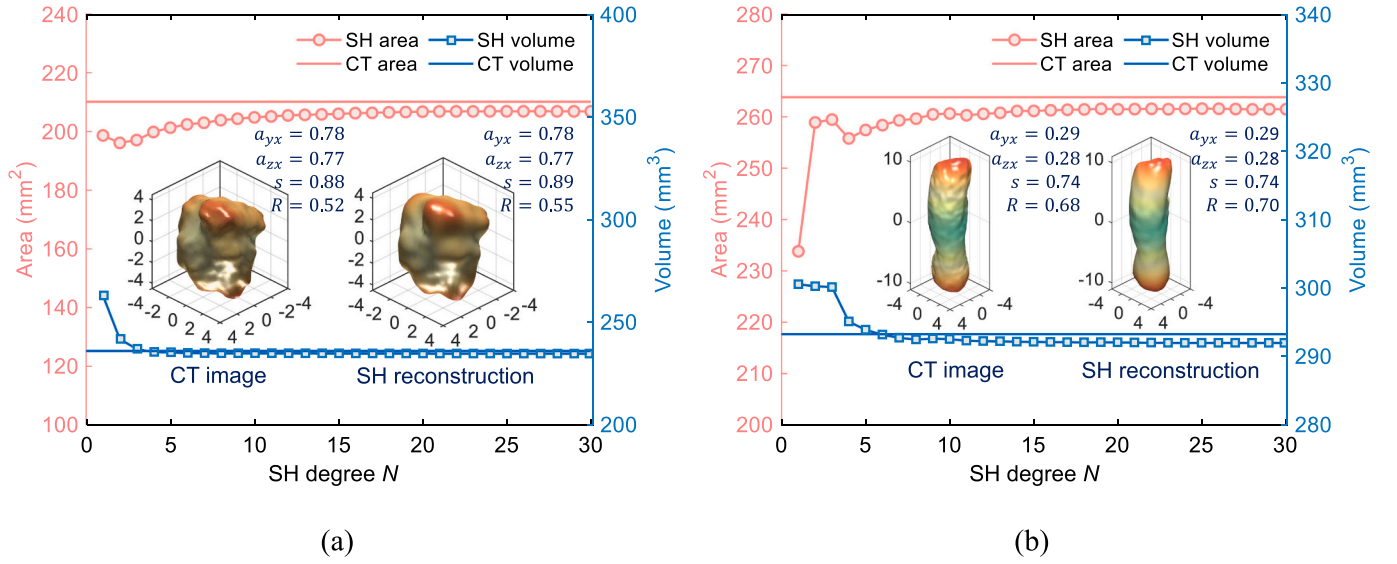


Fig. 10. The volume and surface area of coral sand as a function of SH degree N : (a) lump-like coral sand and (b) stick-like coral sand.

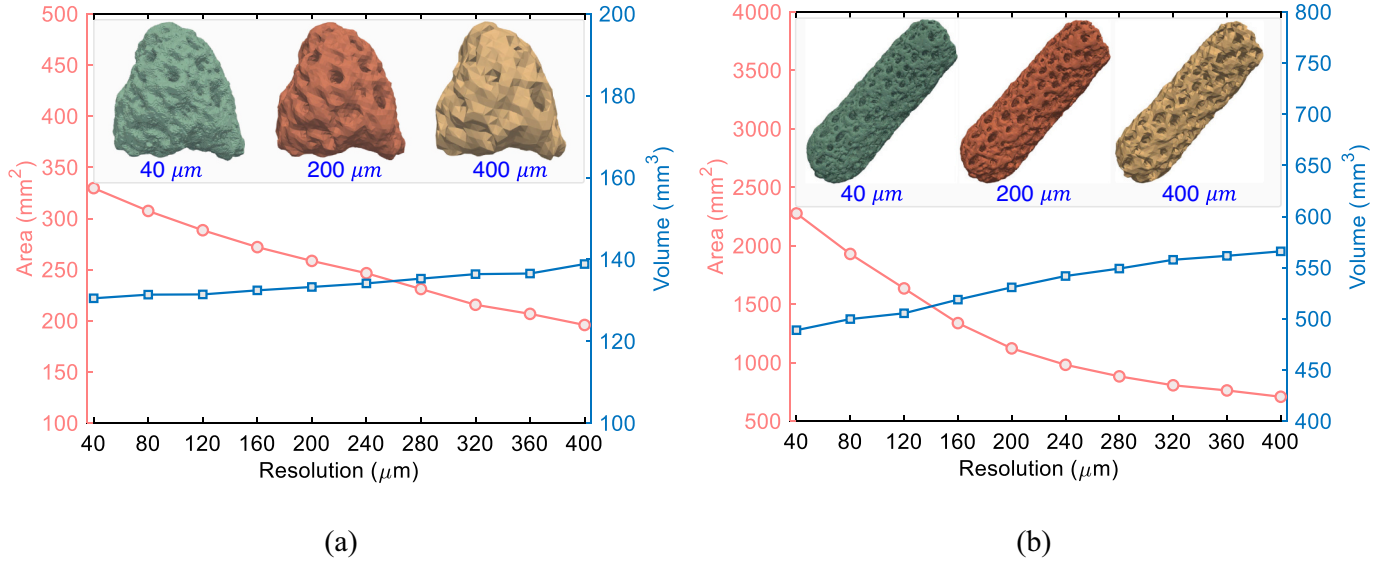


Fig. 11. Surface area and volume of the coral sand as a function of LS resolution: (a) lump-like coral sand and (b) stick-like coral sand.

$\Phi(x_p)$.

The adopted SDF-DEM provides a flexible way to model the apparent shape and internal voids of particles. Specifically, the space with SDF greater than zero is solid, and the space with SDF smaller than zero is void. Within the framework of SDF-DEM, LS is one concrete realization of the SDF-DEM by using a grid of discretized SDF values and their interpolation to define the SDF field. In this work, the LS-based particles are directly created from the CT data of real coral sand particles, and thus the intraparticle voids of coral sand could be captured in high fidelity.

4. Generation of virtual coral sand particles

4.1. RF-SH approach

For a specific type of particles, the SH coefficients of the particles would obey a certain distribution and exhibit a certain correlation with each other. The particle generation problem amounts to generating a set of SH coefficients with a given distribution and correlation. To begin

with, the SH coefficients can be rewritten as a column vector $\mathbf{a} = [a_1, a_2, \dots, a_l]^T$, where $l = (N + 1)^2$ is the total number of SH coefficients for a SH degree of N . The correlation between the SH coefficients is characterized by matrix $\mathbf{C}_{l \times l}$ that

$$\mathbf{C}_{[l \times l]} = \begin{bmatrix} \rho_{a_1, a_1} & \rho_{a_1, a_2} & \cdots & \rho_{a_1, a_l} \\ \rho_{a_2, a_1} & \rho_{a_2, a_2} & \cdots & \rho_{a_2, a_l} \\ \vdots & \vdots & \ddots & \vdots \\ \rho_{a_l, a_1} & \rho_{a_l, a_2} & \cdots & \rho_{a_l, a_l} \end{bmatrix} \quad (26)$$

where the elements ρ_{a_i, a_j} is the correlation between SH coefficients a_i and a_j . With the realistic particle shapes obtained from X-ray CT, SH coefficients can be computed by fitting SH to each particle, and the correlation between each pair of SH coefficients can be calculated by performing the correlation analysis on the samples of SH coefficients. Generally, the magnitudes of SH coefficients decreases significantly with increasing SH degrees. For example, the first-degree SH coefficient, which is closely related to particle size, is significantly greater than the 2nd-, 3rd- and 4th-degree SH coefficients that describe the form of a particle, and far greater than the consecutive higher-degree SH co-

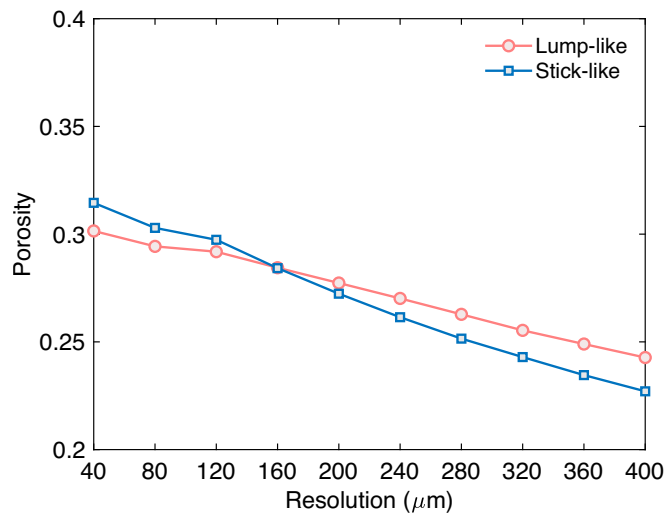


Fig. 12. Internal porosity of the simulated coral sand particles as a function of LS resolution.

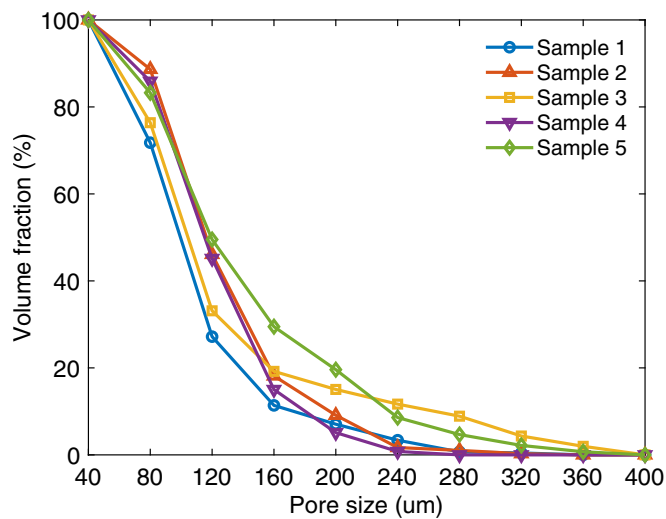
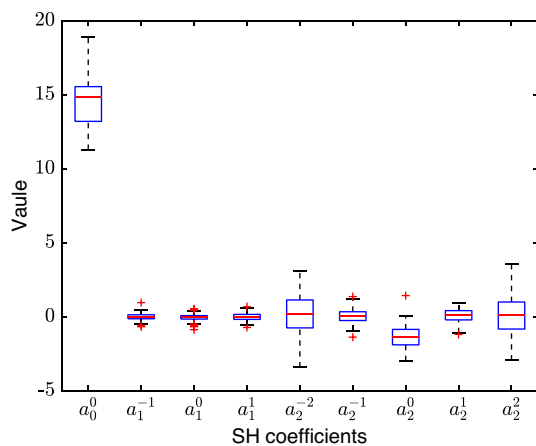
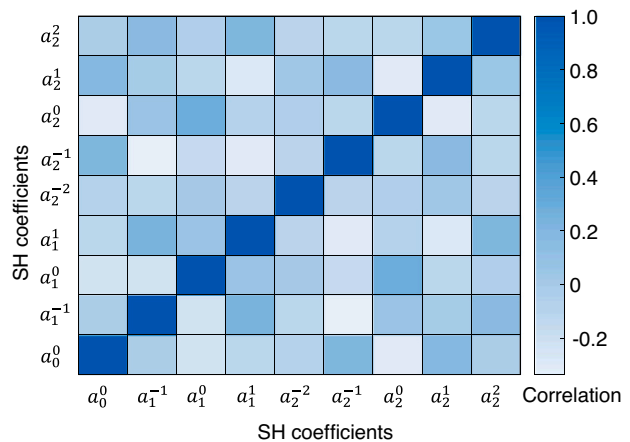


Fig. 13. Pore size distributions of several example coral sand particles.



(a)



(b)

Fig. 14. Statistics (a) of and correlation (b) between several lower-degree SH coefficients of the lump-like coral sand particles.

efficients that capture the roundness and roughness of the particle (Zhou et al., 2015). Thus, the SH coefficients are normalized by their respective maximum value prior to the evaluation of correlation and the RF-based particle generation.

With the distribution and correlation of SH coefficients, random SH coefficients can be generated based on RF theory, such that

$$A = \mu_A + \sigma_A H \tag{27}$$

where A is the generated random SH coefficients; μ_A and σ_A are the mean and standard deviation of the SH coefficients, respectively; and H is a set of correlated random variables with zero mean and unit standard deviation and can be obtained from

$$H = LU \tag{28}$$

where U is a set of independent random variables with zero mean and unit standard deviation, and L is left Cholesky decomposition matrix of the correlation matrix C . It should be pointed out that in this work, the SH coefficients are assumed to obey normal distributions. Other distributions (e.g., fractal distribution (Zhou and Wang, 2017), Gamma distribution (Nie et al., 2020), etc.) can be converted to a normal distribution using the equal probability transformation, where interested readers are referred to Chen et al. (2012) for more details.

4.2. Extend to stick-like particles

The performance of SH degrades when applied to stick-like particles with a large elongation. As it is illustrated in Fig. 6, for fitting an elongated particle, the SH coefficients of some zeroth-order SH terms (i.e., the terms marked with blue box in the figure) would be considerably large, comparing with those of other SH terms. The combination of these zeroth-order SH terms would result in tortuous surface near the particle equator area (marked with red dashed box in the figure). Although the issue of tortuous surface can be mitigated by adopting a higher degree for the SH, higher degree of SH implies greater computational expenses and may not be feasible for numerical modeling.

To extend the SH to elongated particles, a shrinkage strategy is used in this work. The particle is first shrunk in the major principal axis to make it less elongated. Then, SH is applied to the regularized particle. Lastly, the original particle shape is recovered by extending the particle reconstructed from SH with a factor inverse to the shrinkage factor. Herein, the shrinkage factor can be selected such that the particle would have close axis length in each principal direction. It is taken as 0.5 for the stick-like particles being studied in this work. Fig. 7 shows the main

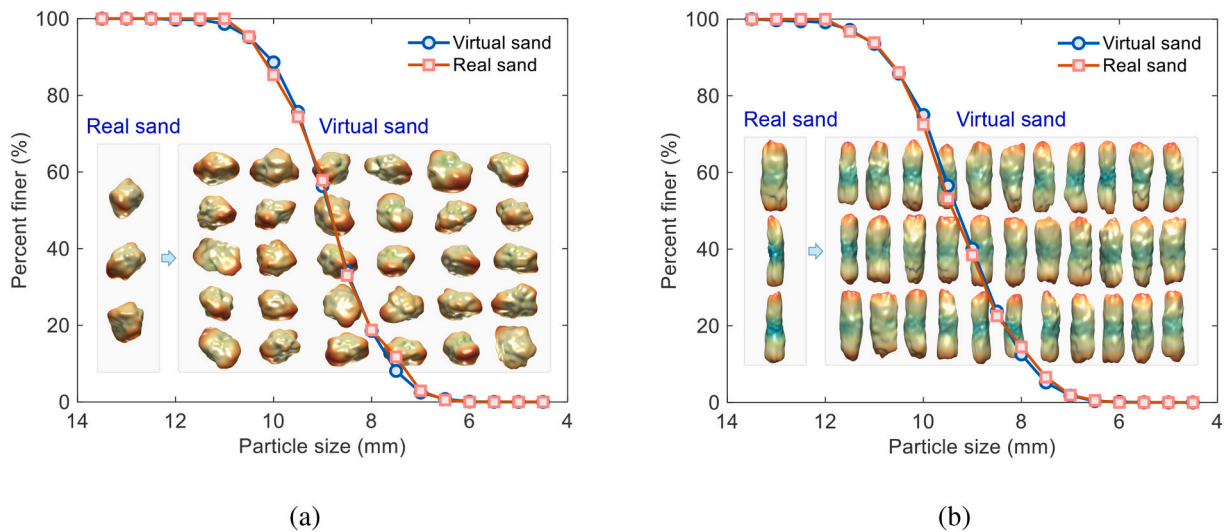


Fig. 15. Particle size distribution of real coral sand and generated virtual coral sand: (a) lump-like coral sand and (b) stick-like coral sand.

steps of this shrinkage strategy. It should be pointed out that by using this shrinkage strategy, the SH coefficients actually represent the surface of a shrunk particle, and thus are not directly applicable to the SDF-DEM presented in Section 3. The RF-SH generated elongated particles could be modeled by other particle models such as LS or polyhedra for SDF-DEM simulation.

5. Results and analysis

This section presents the results and analysis of the morphology and DEM modeling of coral sand, including the accuracy of SH and LS particle models, the effectiveness of RF-SH approach, and DEM simulation of column collapse.

5.1. Accuracy of SH and LS particle models

With the procedures described in Section 2, the morphology of 81 lump-like and 71 stick-like coral sand particles is obtained after X-ray CT scan and imaging processing. The morphology of the particles will be analyzed in the subsequent section, together with the morphology of generated virtual coral sand as comparison. Herein, the accuracy of the SH and LS particle models in representing coral sand is first investigated. Fig. 8 shows two examples of coral sand particles that are represented by SH and LS models, respectively. As aforementioned, the SH particle model is accurate and efficient in describing the overall profile of a particle, whereas the LS particle model is capable of capturing the intraparticle voids. In this regard, both models exhibit fairly good accuracy in representing coral sand particles, without notable differences between the original particles and those represented by SH or LS. Fig. 9 illustrates the difference between the SH particle and LS particle. It is worth noting that LS particles can be seamlessly created from CT scan data, and by the virtue of the property of LS, the LS and CT scan data would give the same particle surface after reconstruction. Thereby, the pore structure from the difference between SH and LS particles would be identical to that from the real CT scan results, if the LS particle is of the same resolution of the CT scan. If a resolution lower than that of the CT scan is used for the LS particle, some pores would be dismissed from the difference between SH and LS particles. As shown in Fig. 9, the pore structure reconstructed based on a resolution of $40\ \mu\text{m}$ could basically capture the geometries and connectivity of the internal pores of the coral sand being studied in this work. The internal porosity is calculated to be about 0.3, which is close to the value reported in the literature (Zhou et al., 2020a). Thus, a resolution of $40\ \mu\text{m}$ is considered to be sufficient for the present study. It is also anticipated that the in-the-majority large

internal pores would dominate the mechanical behavior of coral sand.

Both the SH and LS particle models have a parameter (i.e., degree for SH and grid resolution for LS) that can be flexibly adjusted to weigh a balance between shape representation accuracy and computational efficiency. To investigate the effect of SH degree on the accuracy of SH particle model, a real coral sand particle is fitted by SH with different SH degrees, and the particle volume and surface area are computed to evaluate the shape representation accuracy. Fig. 10 plots the evolution of particle volume and surface area with increasing SH degree. With SH degree lower than 5, the volume and surface area exhibits significant variations, whereas they gradually approach the values of the reference shape (i.e., the shape originally reconstructed from X-ray CT) when the SH degree gets 10 or higher. Thereby, a SH degree of 10 will be used for the subsequent virtual particle generation and DEM simulation. Overall, the results indicate that the highly irregular-shaped coral sand can be well represented by the SH particle model.

Similar to the case of SH particle model, the volume and surface area of particles with different LS resolutions are shown in Fig. 11. In this case, a resolution with smaller values (e.g., $40\ \mu\text{m}$) indicates a high resolution. It is worth noting that the coral sand particles are originally scanned with a resolution of $40\ \mu\text{m}$. The LS-SDF of a particle can be directly obtained from the CT image data of the particles by computing the distance between a voxel and its closest voxel of a different phase. To obtain the LS-SDF with different resolution, the CT image is first re-sized by applying an average filter to the original images. The LS-SDF of a different resolution is then computed from the down-sampled CT images. With increasing resolution (i.e., resolution values varying from $400\ \mu\text{m}$ to $40\ \mu\text{m}$), the particle surface area increases whereas the particle volume decreases. This phenomenon is expected as the voids inside coral sand particles are considerably small comparing to the size of the particle and thus cannot be captured with a low resolution. The intraparticle voids vanish into solids due to the down-sampling process, resulting in increased volume and decreased surface area. It should be noted that, the particle surface area for LS particles includes not only the surface of outer apparent shape but also the surfaces of internal voids.

To investigate further the effect of LS resolution on the intraparticle voids of simulated coral sand particles, the internal porosity and pore size distribution of the simulated particles are analyzed. Fig. 12 plots the average internal porosity of the two types of coral sand particles with different LS resolutions. Overall, the lump-like and stick-like particles present similar internal porosity and trend of evolution with increasing resolution. With the resolution changes from $40\ \mu\text{m}$ to $400\ \mu\text{m}$, the internal porosity decreases from about 0.3 to 0.25, indicating that some intraparticle voids would be dismissed for the cases of low LS resolution.

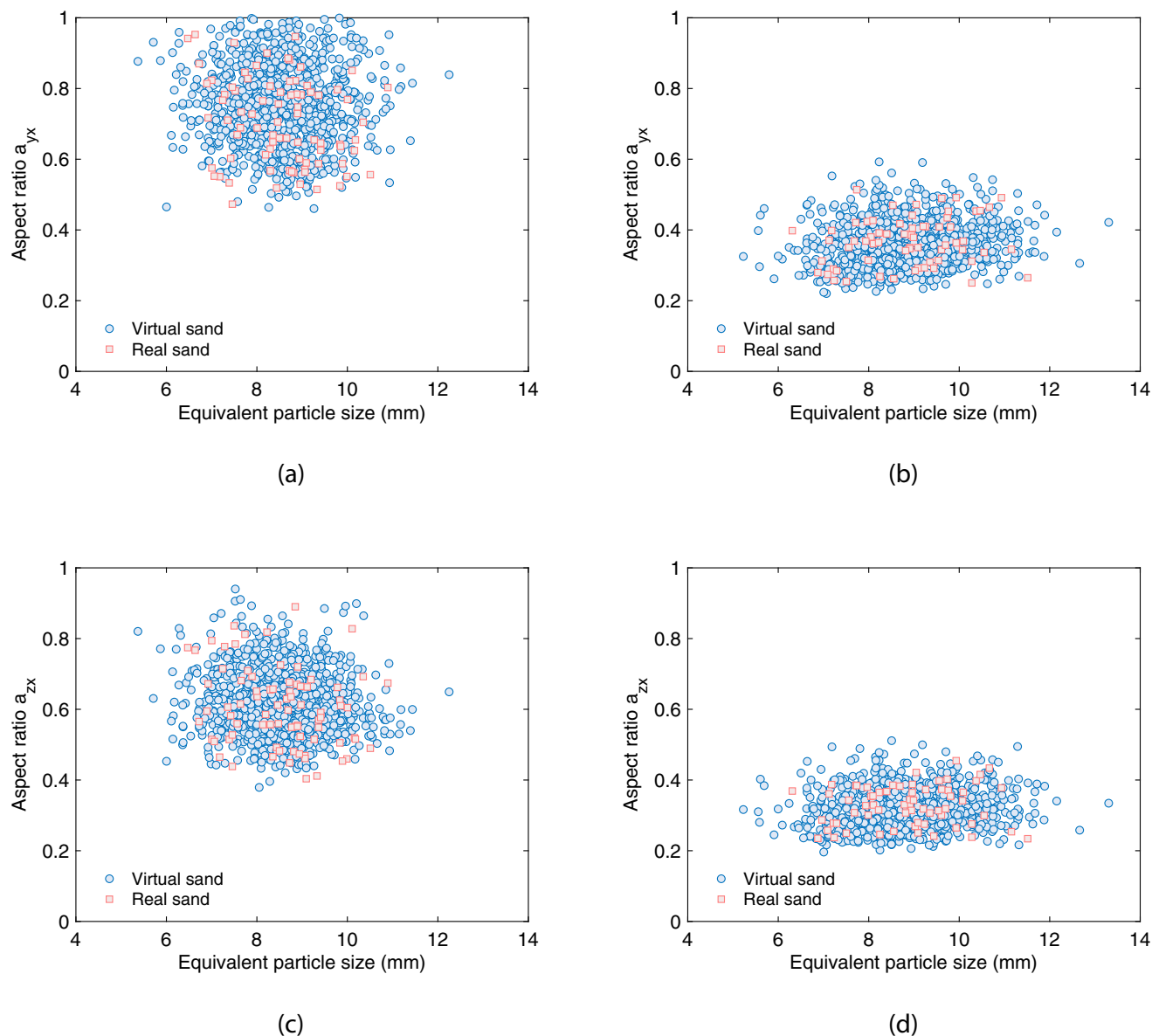


Fig. 16. Aspect ratios of real coral sand and generated virtual coral sand: (a) aspect ratio a_{yx} of lump-like coral sand, (b) aspect ratio a_{yx} of stick-like coral sand, (c) aspect ratio a_{zx} of lump-like coral sand, (d) aspect ratio a_{zx} of stick-like coral sand.

Fig. 13 shows the results of pore size distribution of several example coral sand particles. Herein, the pore sizes of a particle are evaluated using the pore network model in software Avizo. It can be observed from the pore size distribution results that intraparticle voids mainly fall in the size range of $40\ \mu\text{m} \sim 240\ \mu\text{m}$. The results indicate that the intraparticle voids can be reasonably captured by the LS particle model.

To weigh a balance between shape representation accuracy and computation efficiency, the resolution of LS particles will be taken as $200\ \mu\text{m}$ in the following DEM simulations. As it can be observed in Figs. 11 and 13, the LS particles of resolution $200\ \mu\text{m}$ can capture reasonably well the overall profile of the particle and the geometries of intraparticle voids. If the particles of interest have a smaller size or have an abundance of smaller intraparticle voids, higher CT scanning resolution and LS resolution that are comparable to the smallest pore size of interest should be used.

5.2. Effectiveness of RF-SH approach for particle generation

The RF-SH approach for generating virtual coral sand particles that

conform to the morphology characteristics of the real ones has been presented in Section 4. With the morphology of real coral sand particles obtained from CT scan, a point cloud on the surface of a particle is first extracted and used to fit the SH coefficients that describe the particle. Then, the statistics of and correlation between the SH coefficients of all particles are evaluated. For instance, the results of statistics and correlation of several lower-degree SH coefficients of lump-like coral sand particles are shown in Fig. 14. Lastly, new SH coefficients are sampled using the random field theory and thus new virtual coral particles are generated. To investigate the effectiveness of the RF-SH approach for generating coral sand particles, 1,000 particles are generated and compared with real coral sand particles. Fig. 15 plots results of particle size distribution of real coral sand particles and generated virtual particles, which present a pretty good agreement. Herein, the size of a coral sand particle is calculated as the diameter of an equal-volume sphere. In addition, several examples of real particles and virtual particles are embedded in Fig. 15. For both lump-like and stick-like particles, the generated virtual coral sand particles resemble fairly well the real coral sand particles in visual.

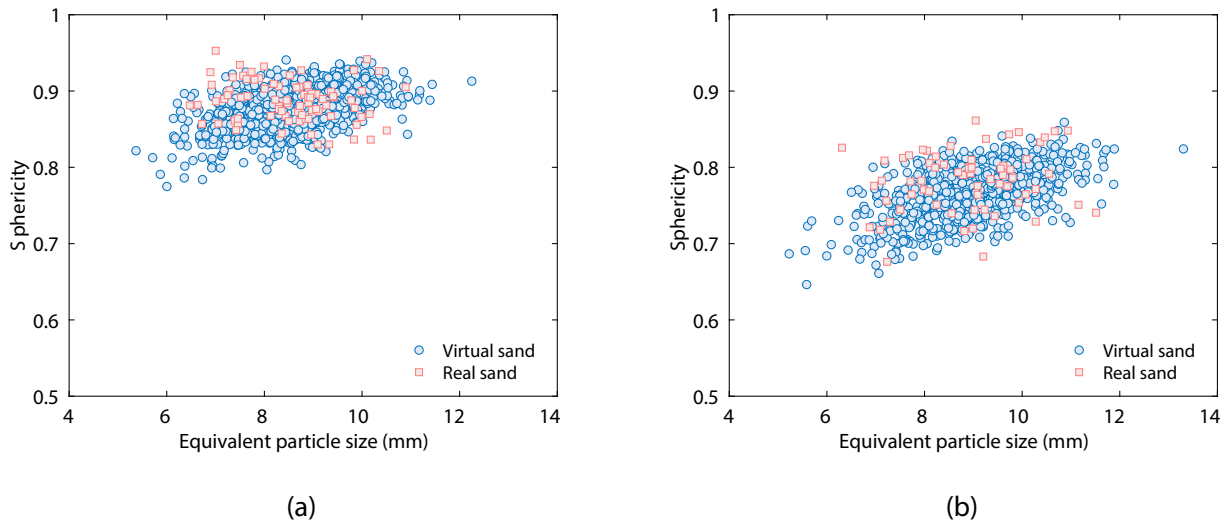


Fig. 17. Sphericity of real coral sand and generated virtual coral sand: (a) lump-like coral sand and (b) stick-like coral sand.

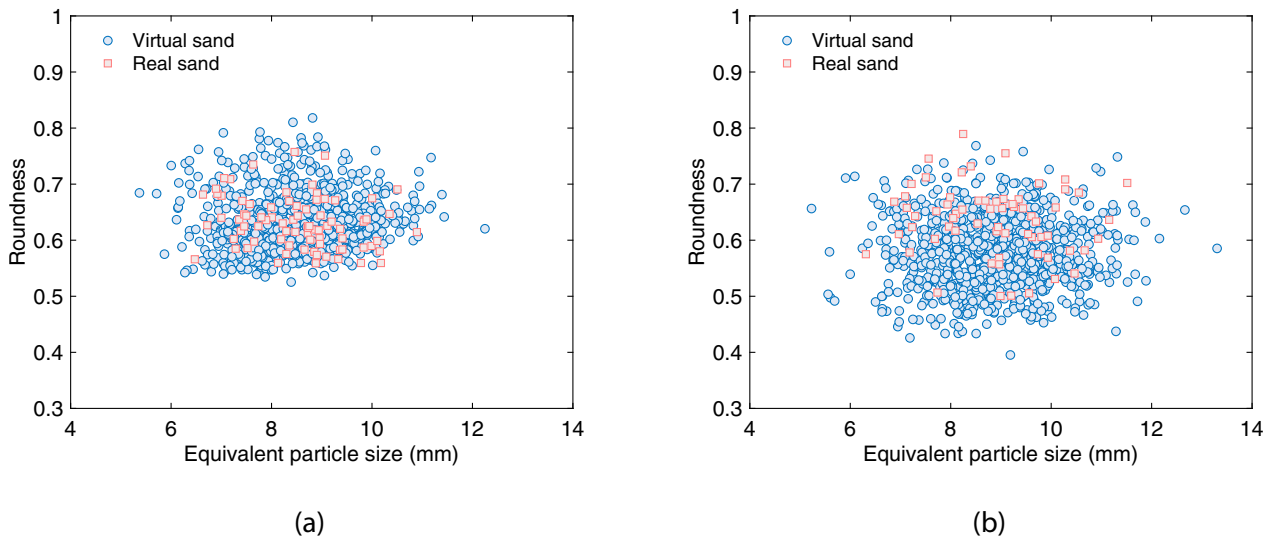


Fig. 18. Roundness of real coral sand and generated virtual coral sand: (a) lump-like coral sand and (b) stick-like coral sand.

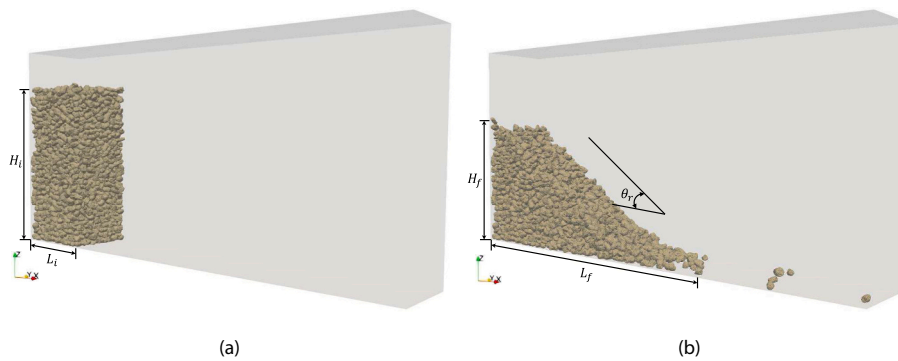


Fig. 19. Particle configurations (a) at initial packing and (b) at the end of collapsing in the DEM simulation of column collapse. H and L , respectively, represent the height and length of the particle packing, subscript i and f indicate initial and final values, respectively, and θ_r is the angle of repose.

As more quantitative analysis, the aspect ratio, sphericity and roundness of the real and virtual coral sand particles are computed, and the results are gathered in Figs. 16–18, respectively. It should be noted that the morphology descriptors are evaluated based on the apparent

shapes of particles, i.e., shapes without intraparticle voids, and thus they quantifies the morphology characteristics of the overall profile of coral sand particles. For lump-like coral sand particles, the aspect ratios a_{yx} and a_{zx} mainly resides in the range 0.5~1.0 and range 0.4~0.8,

Table 1
Model parameters and material properties for the DEM simulation of column collapse test.

Parameter	Value
Particle density ρ	2780 kg/m ³
Contact normal stiffness k_n	2.0×10^5 N/m
Contact shear stiffness k_s	1.0×10^5 N/m
Friction coefficient μ	0.7
Damping coefficient c	0.3
Timestep Δt	1.0×10^{-5} s

Table 2
Simulated repose angle with different contact stiffness, friction coefficient and damping coefficient for lump-like particles with LS-SDF-DEM.

Parameter	Normal stiffness k_n (N/m)	Shear stiffness k_t (N/m)	Damping coefficient (c)	Friction coefficient (μ)	Repose angle (°)
Case R	2×10^5	1×10^5	0.3	0.7	30.1
Case 1	2×10^5	1×10^5	0.3	0.1	15.4
Case 2	2×10^5	1×10^5	0.3	0.3	23.8
Case 3	2×10^5	1×10^5	0.3	0.5	27.4
Case 4	2×10^5	1×10^5	0.3	0.9	30.8
Case 5	2×10^4	1×10^4	0.3	0.7	30.2
Case 6	2×10^6	1×10^6	0.3	0.7	28.6
Case 7	2×10^5	1×10^5	0.7	0.7	29.8

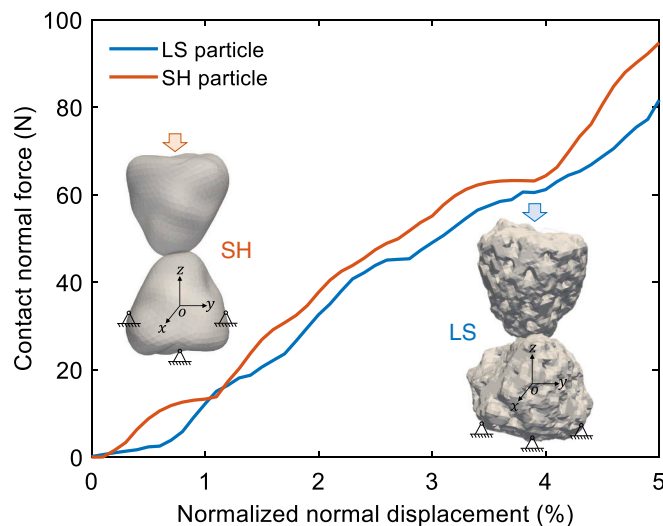


Fig. 20. Force–displacement profile of the contact test on two lump-like coral sand particles. The normal displacement is normalized by the equivalent particle size 0.96 cm.

respectively. The aspect ratios are relatively close to 1.0, indicating that the lump-like coral sand particles do not exhibit great extent of flatness or elongation. By contrast, the aspect ratios of stick-like coral sand particles mainly resides in the range of 0.2~0.5, corresponding to an great extent of elongation. The quantitative results of aspect ratio are consistent with the observed morphology characteristics of coral sand particles in visual. As to the generated virtual coral sand particles, the distributions of aspect ratio also match pretty well with those of real coral sand particles.

Similar to the results of aspect ratio, the results of sphericity and roundness of real coral sand particles are also consistent considerably well with those of virtual particles, as shown in Figs. 17 and 18. The sphericity of lump-like particles are mainly within 0.8~0.95, which is slightly greater than the sphericity (i.e., 0.7~0.85) of stick-like particles. The roundness of lump-like particles is also slightly greater than the

roundness of stick-like particles (i.e., 0.55~0.8 v.s. 0.45~0.75). The results of sphericity and roundness indicate that the lump-like coral sand particles are slightly more spherical and round than stick-like coral sand particles. Overall, the visual and quantitative results of morphology characteristics demonstrate the good effectiveness of the RF-SH approach for generating virtual coral sand particles.

5.3. DEM simulation of column collapse

5.3.1. Simulation setups

In the column collapse test, coral sand particles are first filled into a box container of width 0.1 m and depth 0.08 m. Specifically, packs of particles are repeatedly inserted into the top part of the box and are allowed to settle down under gravity. After insertion, the particles are let relax for one second to reach equilibrium. Then, extra particles are removed so that the particle packing would have the same dimensions as the laboratory experiments. The column eventually has a height of about 0.2 m and consists of about 2,500 particles. After that, the collapse process is proceeded by removing one of the lateral wall of the box container. Fig. 19 illustrates the configurations of particles at initial packing and after collapsing. Similar to the setups of DEM simulation, physical column collapse tests are also conducted in laboratory, where the results are used as benchmark to calibrate and validate the SDF-DEM model for coral sand. Both the lump-like and stick-like coral sand particles will be considered, and in addition, the lump-like coral sand particles are modeled by both the SH and LS particle models, respectively. The SH particles are discretized by 1,000 surface nodes for contact detection and resolution, whereas the LS particles are discretized by 6,000 surface nodes to fully capture the intraparticle voids. The results of SH particle model and LS particle model will be compared with each other to gain insights into the effects of intraparticle voids on the mechanical behavior of coral sand.

The model parameters and material properties for the DEM simulation of column collapse test are listed in Table 1. In particular, the contact stiffness, friction coefficient and damping coefficient are determined through a calibration process. Table 2 presents the results of simulated repose angles of lump-like particles with LS model for the cases of different contact stiffness, friction coefficient and damping coefficient. It can be easily identified that in the column collapse test, the repose angle is mainly affected by the contact friction, whereas the contact stiffness and damping coefficient exhibit negligible influence. For example, with contact friction increases from 0.1 to 0.3, 0.5, and 0.7, the simulated repose angle varies from 15.4° to 23.8°, 27.4°, and 30.1°, respectively. Case R with contact friction 0.7 gives a repose angle that is close to the repose angle of laboratory experiment and is taken as the reference material properties of coral sand.

To gain insight into the contact behavior of coral sand particles modeled in SDF-DEM, a single contact test is performed by gradually pushing one particle towards another. In this case, the two example coral sand particles have an equivalent size of about 0.96 cm. Fig. 20 presents the results of contact normal force with increasing overlapping depth. The force–displacement results exhibit an overall linear profile, indicating that the adopted potential based contact theory with linear contact potential in SDF-DEM can reproduce well the contact behavior of the conventional linear spring contact model.

5.3.2. Runout profile and repose angle

Snapshots of the runout profile of lump-like coral sand particles during the collapsing process are presented in Fig. 21, where the DEM simulation is based on LS particle model. In this case, the intraparticle voids of coral sand particles are directly considered in the DEM simulation. The particles rearrange dramatically during the first 0.6 s and gradually reach equilibrium in less than 5.0 s. It should be noted that the elapsed time of experiments and DEM simulations is the same. Similarly, snapshots of the runout profile of stick-like coral sand particles during the collapsing process are presented in Fig. 22. For stick-like coral sand

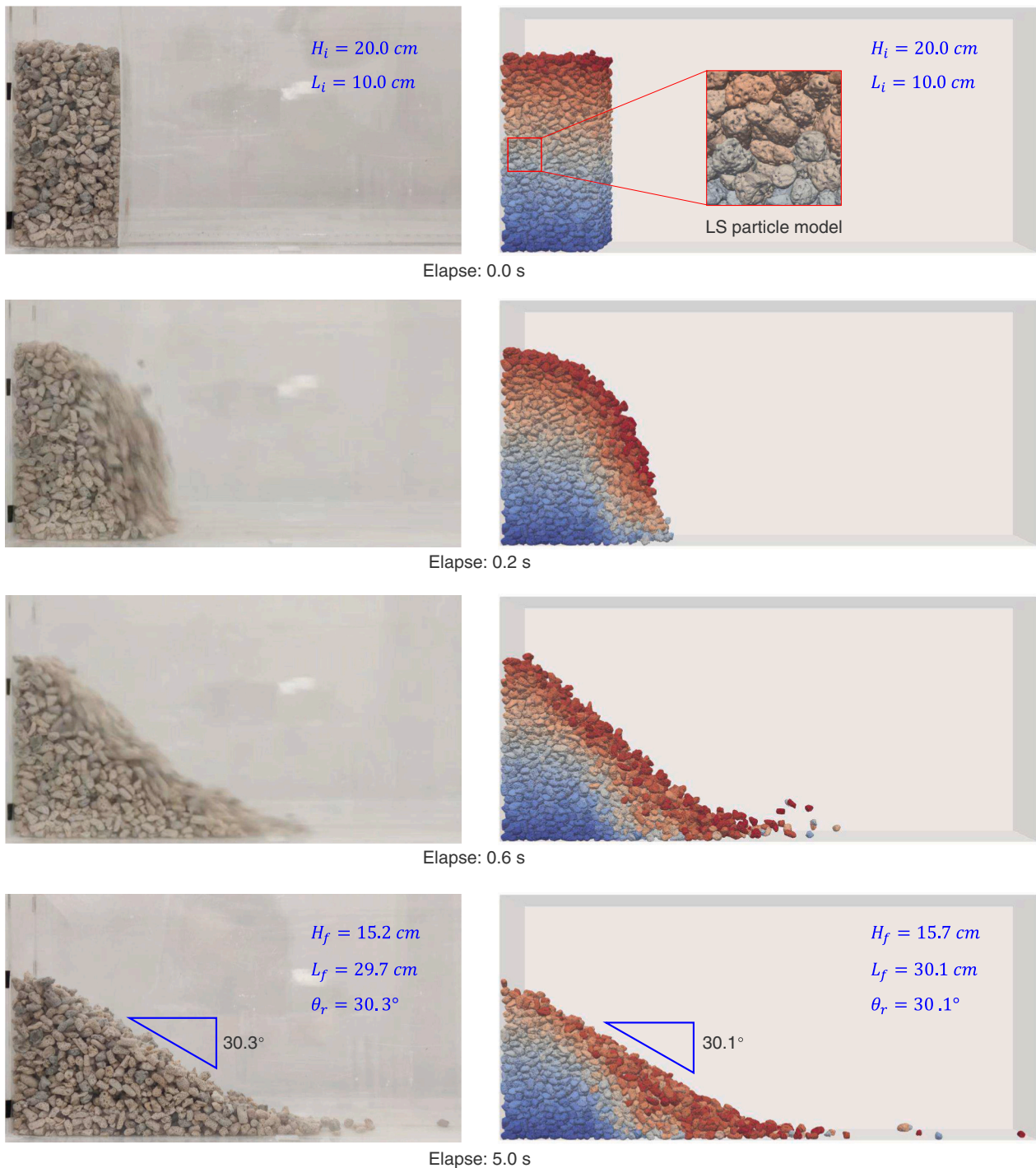


Fig. 21. Snapshots of particle configurations of lump-like coral sand during the collapsing process. The left column shows the experimental results, and the right column shows the LS-SDF-DEM simulation results. The color represents the particle indexes.

particles, the particles exhibit a preference of horizontally laying configuration, i.e., the principal axis of the particles align close with horizon, which is consistent with the laboratory experiments. Most of the particle rearrangements also happens within the beginning 0.6 s. Slightly different from the lump-like case, the bottom portion of the stick-like particles exhibit relatively small amount of rearrangements, which is likely due to the horizontally laying configuration of stick-like particles. In both lump-like and stick-like cases, the runout profiles of LS-SDF-DEM simulation match pretty well with those of laboratory experiment, indicating the good validity and accuracy of the LS-SDF-DEM for modeling coral sand.

For lump-like coral sand particles, column collapse test is also simulated using the SH particle model and the snapshots are presented in Fig. 23. It is observed that the evolution of runout profile simulated based on SH particle model are fairly close to that of LS model. Zoom-in views of the particle configurations at the end of collapsing are presented in Fig. 24. The LS- and SH-based DEM simulations give a repose angle of about 29.6° and 30.1° , which are pretty close to the value 30.3° obtained from laboratory experiment. The results indicate that the intraparticle voids exhibit almost negligible effect on the mechanical behavior of coral sand. It should be noted that no particle breakage is involved in the column collapse test though. As a comparison of the

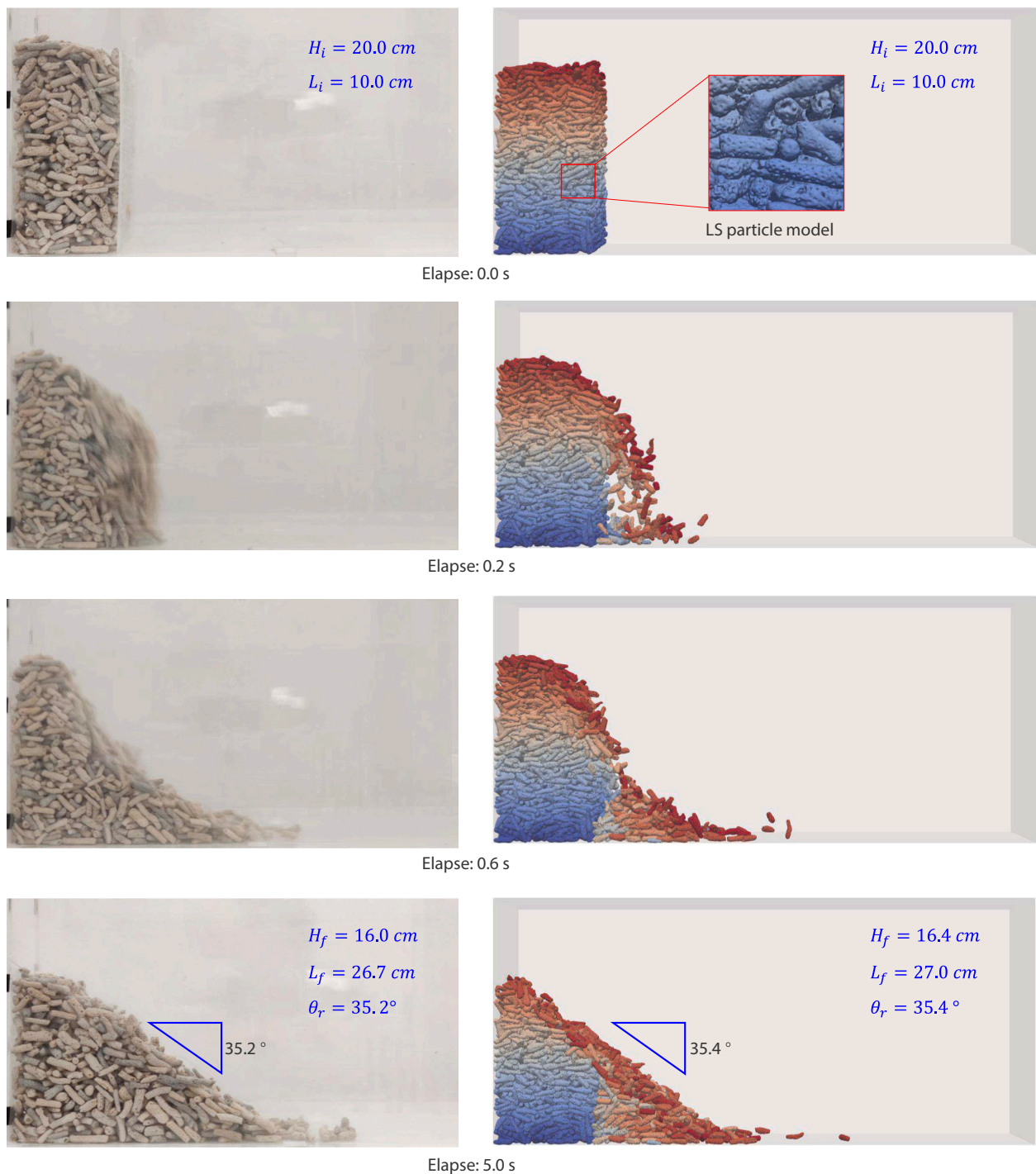


Fig. 22. Snapshots of particle configurations of stick-like coral sand during the collapsing process. The left column shows the experimental results, and the right column shows the LS-SDF-DEM simulation results.

computational performance, the time costs of the LS- and SH-based DEM simulations are about 42.1 h and 18.0 h, respectively, on an Intel i9-10980XE CPU with 32 logic cores. The higher computational cost of LS is mainly due to the larger number (i.e., 6,000 v.s. 1,000 for SH) of surface nodes that are required to capture intraparticle voids of particles. The LS particle model has also a disadvantage that it requires large memory to store the grid of LS values. For the coral sand being studied, the particles have an equivalent size around 7~11 mm, which requires at least 0.34 megabytes to store $35 \times 35 \times 35$ (i.e., 7 mm size by $200 \mu\text{m}$ resolution) double-precision SDF values, whereas it requires only few bytes to store the SH coefficients. In this regard, SH could be used to

model coral sand for computational efficiency and memory saving. Another advantage of the SH particle model is that the SH coefficients could be directly related to the morphology characteristics of a particle, which can be utilized to perform morphology analysis and to generate virtual particles.

5.3.3. Microscopic behaviors

The DEM simulation of coral sand renders it possible to further investigate the microscopic behavior of coral sand particles. To begin with, the average velocity of all particles during the packing, equilibrium and collapsing processes are plotted in Fig. 25. During the packing

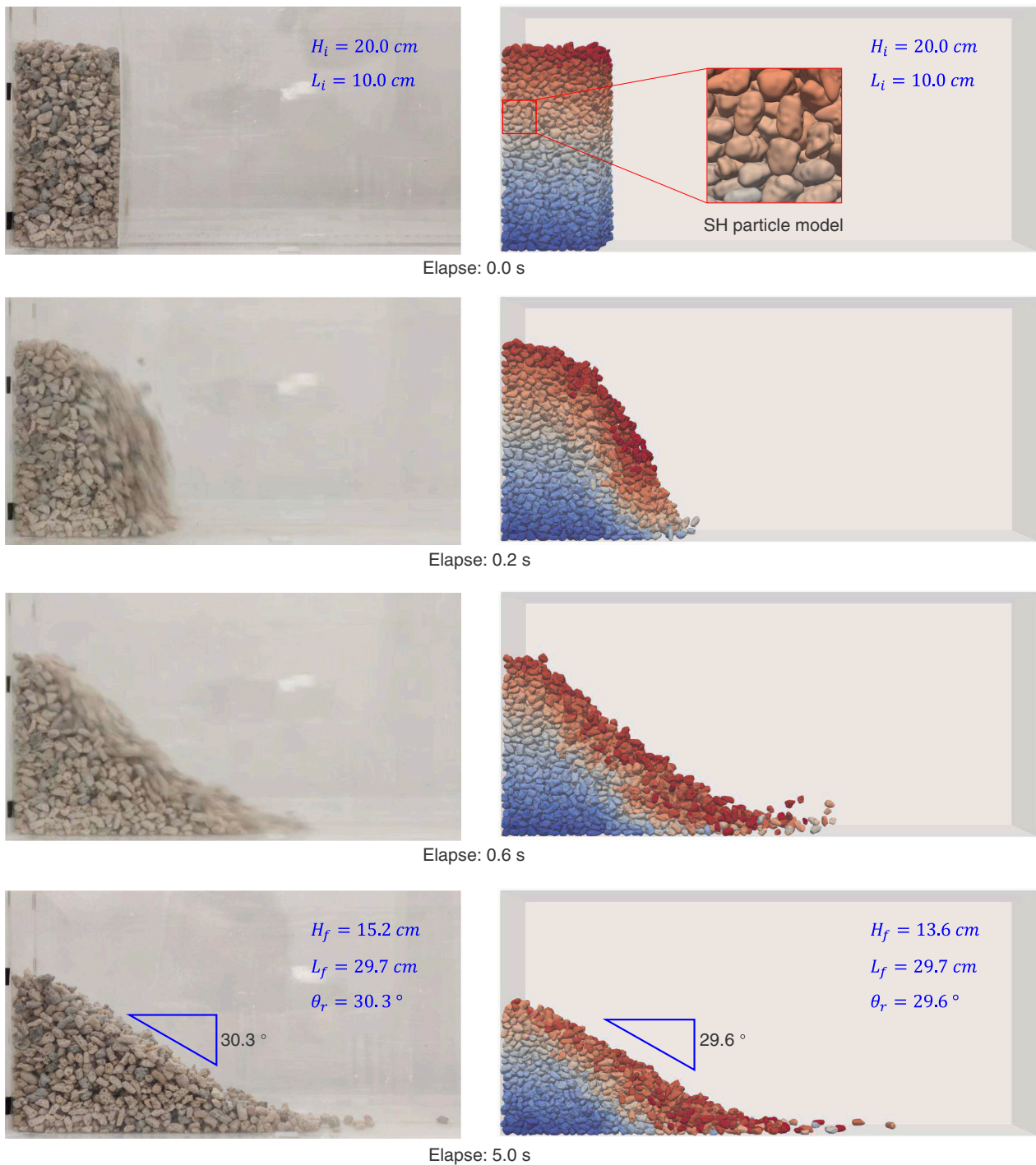


Fig. 23. Snapshots of particle configurations of lump-like coral sand during the collapsing process. The left column shows the experimental results, and the right column shows the SH-SDF-DEM simulation results.

process, the average velocity gradually decreases in a zigzag manner, with each fluctuation corresponding to an event of particle insertion. Within the equilibrium process, the average velocity decreases fast to a relatively small value, indicating a quasi-static equilibrium state. At the onset of collapse, the average velocity exhibits a sudden increase; and it quickly vanishes to a small value in less than 5.0 s when a steady slope is formed. The evolution of average velocity of LS and SH particle models is close to each other. The results demonstrate the good numerical stability of the LS- and SH-SDF-DEM for modeling coral sand.

In addition to particle positions and velocities that can be directly obtained from DEM simulation, secondary information such as packing

fabric and contact force chains can also be evaluated based on the data of particles and contacts. For example, Fig. 26 shows the spherical histogram of the major principal axis of the particles at initial packing and end of collapse. For both the lump-like and stick-like particles, the spherical histograms exhibit an elongated profile in the horizon directions, which is consistent with the deposition profiles visually observed in Figs. 21 and 22. The fabric anisotropy (in terms of the direction of particle principal axes) of stick-like particles is more significant than that of lump-like particles. Fig. 27 compares the contact force chains of lump-like particles and stick-like particles at the end of collapse. No noticeable chains with distinct strong and weak contacts

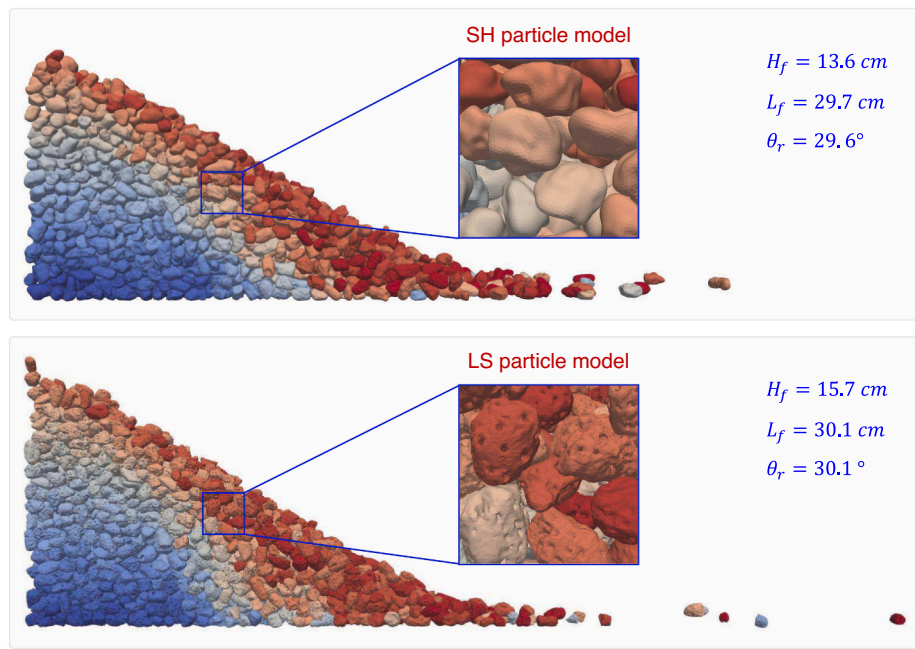


Fig. 24. Snapshots of particle configurations for SH particle model and LS particle model at the end of collapsing.

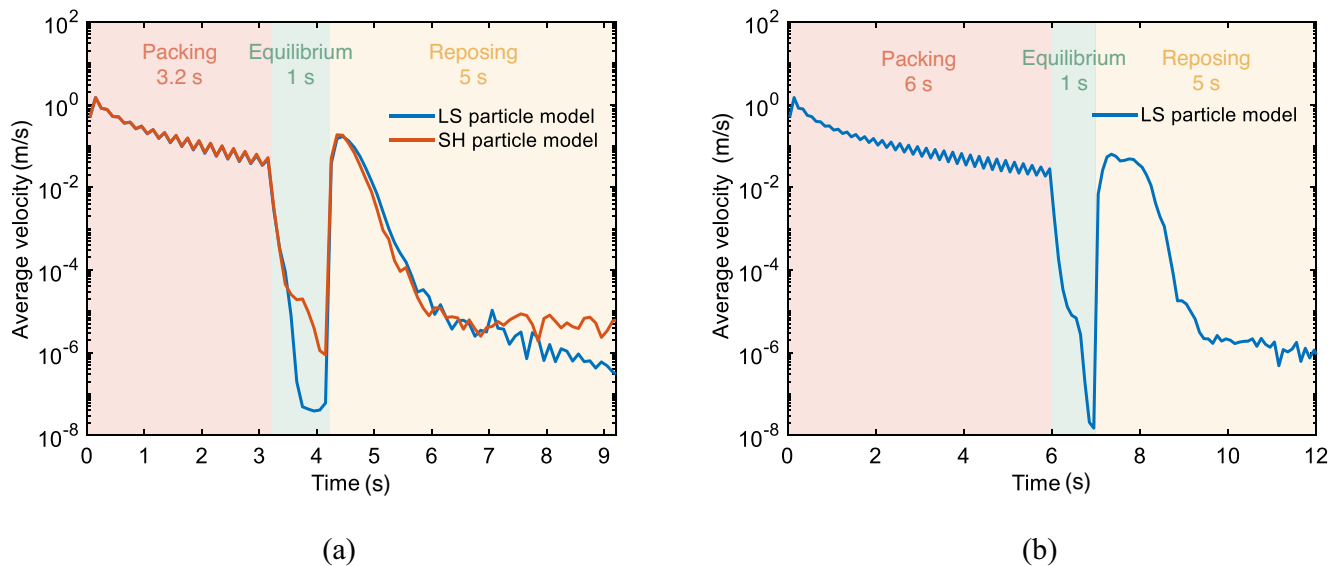


Fig. 25. Evolution of particle average velocity during the packing, equilibrium and collapsing processes in the column collapse test: (a) lump-like coral sand and (b) stick-like coral sand.

can be observed in the figures, indicating that all particles are making a certain contribution to forming such a steady slope. Overall, the macroscopic and microscopic behaviors of coral sand particles demonstrate the good validity, accuracy and numerical stability of the developed and well calibrated SH- and LS-SDF-DEM model for coral sand. It can be applied to simulate and investigate the micro-mechanics of coral sand in more complex conditions, e.g., complex interactions with ocean waves.

It should be noted that the particle breakage effect has not been considered in the present SDF-DEM model for coral sand. Currently, the approaches of breakage modeling in DEM can be mainly categorized into two groups, namely the bonded particle approach (Wu et al., 2019;

Wu et al., 2022; Peng et al., 2022) and the particle replacement approach (Tavares et al., 2021; Hu et al., 2021). In the bonded particle approach, a set of child particles are bonded together to form a large parent particle, and particle breakage is modeled by considering the failure of the bonds between child particles. For the particle replacement approach, the breakage of a particle is determined by testing a given failure criterion (Tavares et al., 2021) or performing a separate numerical modeling (e.g., using peridynamics (Zhu and Zhao, 2019), material point method (Xiao et al., 2021) or FDEM). A broken particle would then be replaced with a set of newly generated child particles. The present SDF-DEM has the advantage of modeling irregular-shaped particles, providing a flexible way to model the irregular-shaped particle

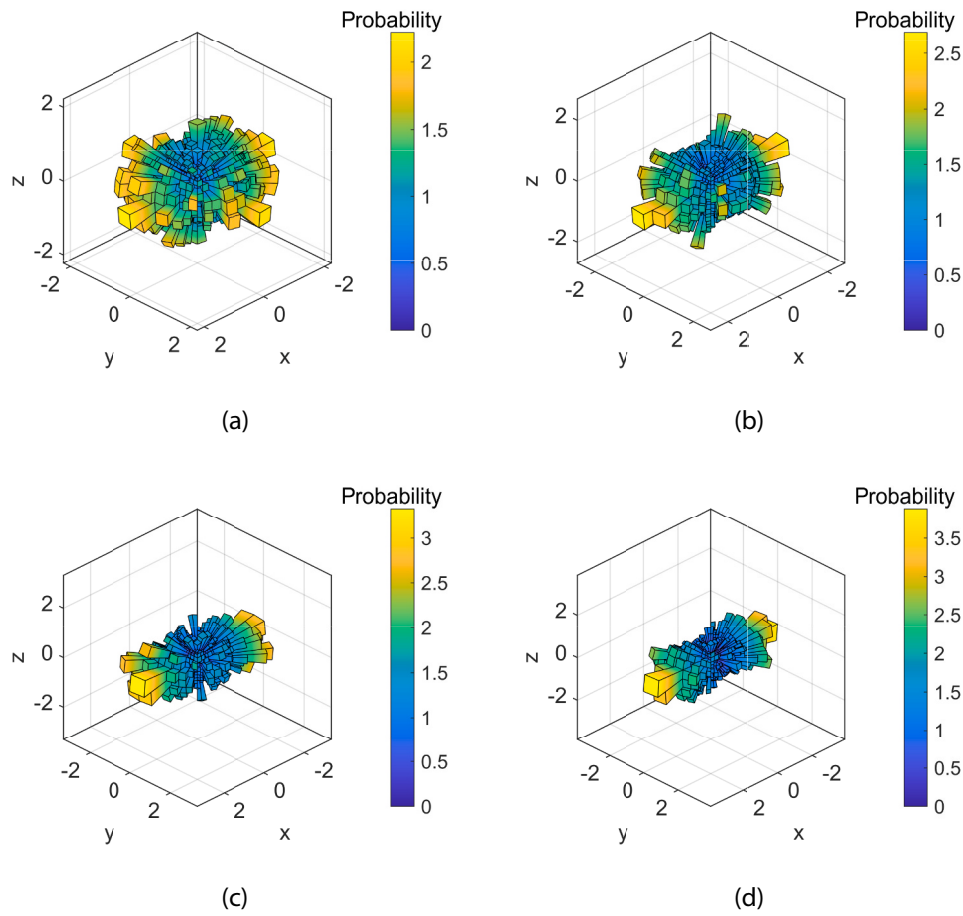


Fig. 26. Distribution of the directions of particle major principal axis at initial packing and end of collapsing: (a) lump-like particles at initial packing, (b) lump-like particles at end of collapsing, (c) stick-like particles at initial packing, and (d) stick-like particles at end of collapsing.

fragments for both approaches. Particularly, there is a recent work that integrates the LS particle model with the domain splitting approach to model particle breakage (Harmon et al., 2020). This approach is also palatable to the present SDF-DEM framework and its application to coral sand particles will be explored in future.

6. Conclusions

This work presented a signed distance field-based DEM (SDF-DEM) for the numerical modeling of coral sand in consideration of both the irregular shapes and intraparticle voids of coral sand particles. The SDF-DEM features in using an SDF to represent particles, making it applicable to any irregular geometries. Within the SDF-DEM, two versatile particle models are introduced for modeling coral sand particles, namely spherical harmonics (SH) and level set (LS). SH is efficient and accurate in describing the apparent shapes of coral sand particles, whereas LS is capable of capturing the voids inside particles. To create the DEM model for coral sand, the X-ray CT technique and image processing procedures for acquisition and characterization of the morphology of realistic coral sand particles are described. In particular, two types of image processing schemes are introduced, with one including intraparticle voids and the other not. The former scheme is palatable to LS particle model, whereas the latter one would be favored by SH particle model. Furthermore, the RF-SH approach for generating virtual coral sand particles and the remedy to elongated particles are also presented. Based on the SDF-DEM and the morphology of realistic coral sand, DEM simulations of column collapse of coral sand are performed and compared with laboratory experiments. Main findings of this work are summarized as follows:

1. Both SH and LS particle models are applicable to coral sand. The shape representation accuracy increases with SH degree and LS resolution, where an SH degree of 10 and LS resolution of about 200 μm are sufficient to approach towards an accurate representation of coral sand particles.
2. The RF-SH approach exhibits pretty good effectiveness in generating virtual coral sand particles, including both the lump-like and stick-like ones. The distributions of the morphology, in terms of equivalent size, aspect ratio, sphericity, and roundness, of realistic and generated virtual coral sand particles agree well with each other.
3. The calibrated SDF-DEM model shows fairly good performance in the DEM simulation of coral sand. The lump-like coral sand exhibits a repose angle of about 30.3° , slightly lower than that (i.e., 35.2°) of the stick-like one. The runout profiles and repose angle obtained from DEM simulation match well with those from laboratory experiments.
4. SH and LS particle models present similar results in the column collapse DEM simulations, indicating that the intraparticle voids exhibit a fairly negligible effect on the mechanical behavior of coral sand, in the cases where no breakage is involved. In this regard, SH could be used to model coral sand for computational efficiency and memory saving.

The workflow for the morphology characterization and the tool for numerical modeling of coral sand developed in this work would facilitate the fundamental understanding and application of coral sand in engineering. Based on the well developed and calibrated DEM model, the mechanical behavior of coral sand in practical problems (e.g.,

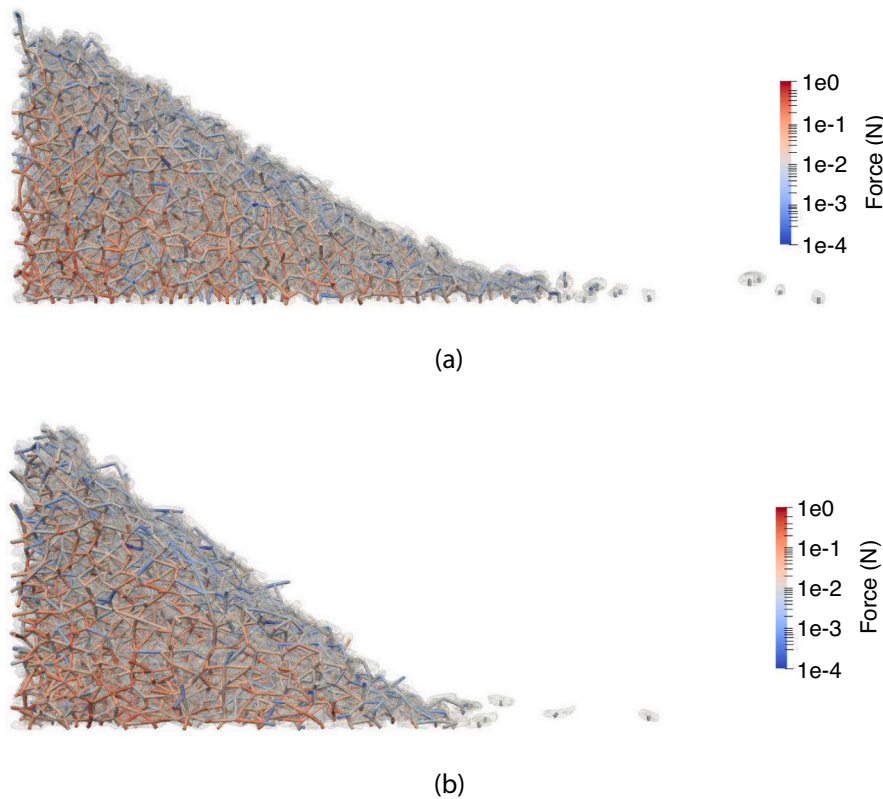


Fig. 27. Contact force chains of (a) lump-like particles and (b) stick-like particles at the end of collapsing.

erosion and suffusion) with more complex environment and loading conditions could be investigated in the future.

CRediT authorship contribution statement

Shuai Huang: Data-curation, Formal-analysis, Visualization, Writing-original-draft. **Linchong Huang:** Resources, Supervision, Project-administration, Writing-review-editing. **Zhengshou Lai:** Conceptualization, Methodology, Software, Writing-review-editing. **Jidong Zhao:** Supervision, Writing-review-editing.

Declaration of Competing Interest

The authors declare that they have no known competing financial interests or personal relationships that could have appeared to influence the work reported in this paper.

Data availability

Data will be made available on request.

Acknowledgments

This work has been financially supported by the Hong Kong Scholars Program (2020), the National Natural Science Foundation of China (51909289, 51978677, 52111530089), the Shenzhen Science and Technology Project for Sustainable Development (KCFZ202002011008532), the Shenzhen Natural Science Foundation (JCYJ20190807162401662), the Project of Hetao Shenzhen-Hong Kong Science and Technology Innovation Cooperation Zone (HZQB-KCZYB-2020083), and the Research Grants Council of Hong Kong (16211221).

References

- Alba, J., Audibert, J., 1999. Pile design in calcareous and carbonaceous granular materials, and historic review. In: Proceedings of the 2nd international conference on engineering for calcareous sediments, vol. 1. AA Balkema, Rotterdam, pp. 29–44.
- Andò, E., Viggiani, G., Hall, S., Desrues, J., 2013. Experimental micro-mechanics of granular media studied by X-ray tomography: recent results and challenges. *Geotechn. Lett.* 3 (3), 142–146.
- Balevičius, R., Mróz, Z., 2013. A finite sliding model of two identical spheres under displacement and force control – part I: static analysis. *Acta Mech.* 224 (8), 1659–1684.
- Capozza, R., Hanley, K.J., 2021. A hierarchical, spherical harmonic-based approach to simulate abradable, irregularly shaped particles in DEM. *Powder Technol.* 378, 528–537.
- Chen, Q., Seifried, A., Andrade, J.E., Baker, J.W., 2012. Characterization of random fields and their impact on the mechanics of geosystems at multiple scales. *Int. J. Numer. Anal. Meth. Geomech.* 36 (2), 140–165.
- Feng, Y.T., 2021a. An effective energy-conserving contact modelling strategy for spherical harmonic particles represented by surface triangular meshes with automatic simplification. *Comput. Methods Appl. Mech. Eng.* 379, 113750.
- Feng, Y.T., 2021b. An energy-conserving contact theory for discrete element modelling of arbitrarily shaped particles: Basic framework and general contact model. *Comput. Methods Appl. Mech. Eng.* 373, 113454.
- Garboczi, E.J., 2011. Three dimensional shape analysis of JSC-1A simulated lunar regolith particles. *Powder Technol.* 207 (1–3), 96–103.
- Harmon, J.M., Arthur, D., Andrade, J.E., 2020. Level set splitting in DEM for modeling breakage mechanics. *Comput. Methods Appl. Mech. Eng.* 365, 112961.
- Hu, F., Fang, X., Yao, Z., Wu, H., Shen, C., Zhang, Y., 2021. Experiment and discrete element modeling of particle breakage in coral sand under triaxial compression conditions. *Mar. Georesources Geotechnol.* 1–10.
- Johnson, K.L., 1987. *Contact mechanics*. Cambridge University Press.
- Kawamoto, R., Andò, E., Viggiani, G., Andrade, J.E., 2016. Level set discrete element method for three-dimensional computations with triaxial case study. *J. Mech. Phys. Solids* 91, 1–13.
- Kawamoto, R., Andò, E., Viggiani, G., Andrade, J.E., 2018. All you need is shape: Predicting shear banding in sand with LS-DEM. *J. Mech. Phys. Solids* 111, 375–392.
- King, R.W., 1980. GEOTECHNICAL ASPECTS OF FOUNDATION INVESTIGATIONS FOR PRODUCTION PLATFORMS AT North Rankin. *APPEA J.* 20 (1), 257–262.
- Kong, D., Fonseca, J., 2018. Quantification of the morphology of shelly carbonate sands using 3D images. *Geotechnique* 68 (3), 249–261.
- Kong, D., Fonseca, J., 2019. On the kinematics of shelly carbonate sand using X-ray micro tomography. *Eng. Geol.* 261, 105268.

- Kuang, D., Long, Z., Guo, R., Yu, P., 2021. Experimental and numerical investigation on size effect on crushing behaviors of single calcareous sand particles. *Mar. Georesources Geotechnol.* 39 (5), 543–553.
- Lade, P.V., Liggio, C.D., Nam, J., 2009. Strain Rate, Creep, and Stress Drop-Creep Experiments on Crushed Coral Sand. *J. Geotech. Geoenviron. Eng.* 135 (7), 941–953.
- Lai, Z., Chen, Q., 2019. Reconstructing granular particles from X-ray computed tomography using the TWS machine learning tool and the level set method. *Acta Geotech.* 14, 1–18.
- Lai, Z., Zhao, S., Zhao, J., Huang, L., 2022. Signed distance field framework for unified DEM modeling of granular media with arbitrary particle shapes. *Comput. Mech.* 70 (4), 763–783.
- Lu, Z., Hou, H., Jiang, P., Wang, Q., Li, T., Pan, Z., 2022. Three-Dimensional Discrete Element Analysis of Crushing Characteristics of Calcareous Sand Particles. *Geofluids* 2022, 1–9.
- Lv, Y., Li, X., Fan, C., Su, Y., 2021. Effects of internal pores on the mechanical properties of marine calcareous sand particles. *Acta Geotech.* 16 (10), 3209–3228.
- Ma, G., Xiao, Y., Fan, W., Chu, J., Liu, H., 2022. Mechanical properties of biocement formed by microbially induced carbonate precipitation. *Acta Geotech.* 1–15.
- Mollon, G., Zhao, J., 2014. 3D generation of realistic granular samples based on random fields theory and Fourier shape descriptors. *Comput. Methods Appl. Mech. Eng.* 279 (sep.1), 46–65.
- Nie, J.Y., Li, D.Q., Cao, Z.J., Zhou, B., Zhang, A.J., 2020. Probabilistic characterization and simulation of realistic particle shape based on sphere harmonic representation and Nataf transformation. *Powder Technol.* 360, 209–220.
- Pac, S., 1978. Coral-reef area and the contributions of reefs to processes and resources of the world's oceans. *Nature* 273, 18.
- Peng, J., Wong, L.N.Y., Teh, C.I., 2018. A re-examination of slenderness ratio effect on rock strength: Insights from DEM grain-based modelling. *Eng. Geol.* 246, 245–254.
- Peng, Y., Ding, X., Yin, Z.-Y., Wang, P., 2022. Micromechanical analysis of the particle corner breakage effect on pile penetration resistance and formation of breakage zones in coral sand. *Ocean Eng.* 259, 111859.
- PFCD documentation, 2021. <http://docs.itascacg.com/pfc700/contents.html>, accessed: 2021-06-30.
- Qin, Y., Xu, D., Fan, X., 2022. Effect of pile inclination on the lateral deformation behaviour of pipe piles in calcareous sand. *Mar. Georesources Geotechnol.* 40 (5), 589–599.
- Rui, S., Guo, Z., Si, T., Li, Y., 2020. Effect of particle shape on the liquefaction resistance of calcareous sands. *Soil Dyn. Earthq. Eng.* 137, 106302.
- Salem, M., Elmamlouk, H., Agaiby, S., 2013. Static and cyclic behavior of North Coast calcareous sand in Egypt. *Soil Dyn. Earthquake Eng.* 55, 83–91.
- Shahnazari, H., Rezvani, R., 2013. Effective parameters for the particle breakage of calcareous sands: An experimental study. *Eng. Geol.* 159, 98–105.
- Shi, D.D., Cao, D., Deng, Y.B., Xue, J.F., 2021a. DEM investigations of the effects of intermediate principal stress ratio and particle breakage on the critical state behaviors of granular soils. *Powder Technol.* 379, 547–559.
- Shi, J., Zhang, W., Wang, W., Sun, Y., Xu, C., Zhu, H., Sun, Z., 2021b. Randomly generating three-dimensional realistic schistous sand particles using deep learning: Variational autoencoder implementation. *Eng. Geol.* 291, 106235.
- Su, D., Yan, W.M., 2018. 3D characterization of general-shape sand particles using microfocus X-ray computed tomography and spherical harmonic functions, and particle regeneration using multivariate random vector. *Powder Technol.* 323, 8–23.
- Tavares, L.M., Rodriguez, V.A., Sousani, M., Padros, C.B., Ooi, J.Y., 2021. An effective sphere-based model for breakage simulation in DEM. *Powder Technol.* 392, 473–488.
- Wadell, H., 1933. Sphericity and roundness of rock particles. *J. Geol.* 41 (3), 310–331.
- Wang, X., Jiao, Y., Wang, R., Hu, M., Meng, Q., Tan, F., 2011. Engineering characteristics of the calcareous sand in Nansha Islands, South China Sea. *Eng. Geol.* 120 (1–4), 40–47.
- Wang, X., Wang, X., Jin, Z., Zhu, C., Wang, R., Meng, Q., 2017. Investigation of engineering characteristics of calcareous soils from fringing reef. *Ocean Eng.* 134, 77–86.
- Wang, X., Weng, Y., Wei, H., Meng, Q., Hu, M., 2019a. Particle obstruction and crushing of dredged calcareous soil in the Nansha Islands, South China Sea. *Eng. Geol.* 261, 105274.
- Wang, Y., Zhou, L., Yang, Q., 2019b. Hydro-mechanical analysis of calcareous sand with a new shape-dependent fluid-particle drag model integrated into CFD-DEM coupling program. *Powder Technol.* 344, 108–120.
- Wang, J., Fan, P., Wang, M., Dong, L., Ma, L., Gao, L., 2020a. Experimental study of one-dimensional compression creep in crushed dry coral sand. *Can. Geotech. J.* 57 (12), 1854–1869.
- Wang, X., Wu, Y., Cui, J., Zhu, C.-Q., Wang, X.-Z., 2020b. Shape characteristics of coral sand from the South China Sea. *J. Mar. Sci. Eng.* 8 (803), 1–24.
- Wang, X., Yin, Z.-Y., Xiong, H., Su, D., Feng, Y.-T., 2021a. A spherical-harmonic-based approach to discrete element modeling of 3D irregular particles. *Int. J. Numer. Meth. Eng.* 122 (20), 5626–5655.
- Wang, X., Nie, Z., Gong, J., Liang, Z., 2021b. Random generation of convex aggregates for DEM study of particle shape effect. *Constr. Build. Mater.* 268, 121468.
- Wei, H., Zhao, T., Meng, Q., Wang, X., Zhang, B., 2020. Quantifying the morphology of calcareous sands by dynamic image analysis. *Int. J. Geomech.* 20 (4), 04020020.
- Wu, H., Zhao, J., Guo, N., 2019. Multiscale modeling of compaction bands in saturated high-porosity sandstones. *Eng. Geol.* 261, 105282.
- Wu, Q., Ding, X., Zhang, Y., Chen, Z., Zhang, Y., 2021. Numerical simulations on seismic response of soil-pile-superstructure in coral sand. *Ocean Eng.* 239, 109808.
- Wu, H., Wu, W., Liang, W., Dai, F., Liu, H., Xiao, Y., 2022. 3D DEM modeling of biocemented sand with fines as cementing agents. *Int. J. Numer. Anal. Meth. Geomech.* 1–29.
- Xiao, M., Liu, C., Sun, W., 2021. DP-MPM: Domain partitioning material point method for evolving multi-body thermal-mechanical contacts during dynamic fracture and fragmentation. *Comput. Methods Appl. Mech. Eng.* 385, 114063.
- Xiao, Y., Wang, C., Shi, J., Long, L., Liu, H., 2022. Fracturing and Ultimate State of Binary Carbonate Sands. *Int. J. Geomech.* 22 (7), 04022089.
- Xu, S., Zhu, Y., Cai, Y., Sun, H., Cao, H., Shi, J., 2022. Predicting the permeability coefficient of polydispersed sand via coupled CFD-DEM simulations. *Comput. Geotech.* 144, 104634.
- Yu, D., Ye, J., Yao, L., 2020. Prediction of the long-term settlement of the structures built on a reclaimed coral reef island: an aircraft runway. *Bull. Eng. Geol. Environ.* 79 (9), 4549–4564.
- Zhao, L., Zhang, S., Huang, D., Wang, X., Zhang, Y., 2020. 3D shape quantification and random packing simulation of rock aggregates using photogrammetry-based reconstruction and discrete element method. *Constr. Build. Mater.* 262, 119986.
- Zheng, J., Hryciw, R.D., 2017. Soil particle size and shape distributions by stereophotography and image analysis. *Geotech. Test. J.* 40 (2), 317–328.
- Zhou, B., Wang, J., 2017. Generation of a realistic 3D sand assembly using X-ray micro-computed tomography and spherical harmonic-based principal component analysis. *Int. J. Numer. Anal. Meth. Geomech.* 41 (1), 93–109.
- Zhou, B., Wang, J., Zhao, B., 2015. Micromorphology characterization and reconstruction of sand particles using micro X-ray tomography and spherical harmonics. *Eng. Geol.* 184, 126–137.
- Zhou, B., Wang, J., Wang, H., 2018a. Three-dimensional sphericity, roundness and fractal dimension of sand particles. *Geotechnique* 68 (1), 18–30.
- Zhou, B., Wang, J., Wang, H., 2018b. A novel particle tracking method for granular sands based on spherical harmonic rotational invariants. *Geotechnique* 68 (12), 1116–1123.
- Zhou, B., Ku, Q., Wang, H., Wang, J., 2020a. Particle classification and intra-particle pore structure of carbonate sands. *Eng. Geol.* 279, 105889.
- Zhou, B., Wei, D., Ku, Q., Wang, J., Zhang, A., 2020b. Study on the effect of particle morphology on single particle breakage using a combined finite-discrete element method. *Comput. Geotech.* 122, 103532.
- Zhou, B., Ku, Q., Li, C., Wang, H., Dong, Y., Cheng, Z., 2022. Single-particle crushing behaviour of carbonate sands studied by X-ray microtomography and a combined finite-discrete element method. *Acta Geotech.* 1–15.
- Zhu, F., Zhao, J., 2019. Modeling continuous grain crushing in granular media: a hybrid peridynamics and physics engine approach. *Comput. Methods Appl. Mech. Eng.* 348, 334–355.